Towards a Better Understanding of the Na-O_2 Battery System

by

Russel Xavier Fernandes

A thesis

presented to the University of Waterloo

in fulfillment of the

thesis requirement for the degree of

Master of Science

in

Chemistry (Nanotechnology)

Waterloo, Ontario, Canada, 2016

AUTHOR'S DECLARATION

I hereby declare that I am the sole author of this thesis. This is a true copy of the thesis, including any required final revisions, as accepted by my examiners.

I understand that my thesis may be made electronically available to the public.

_____

Russel Xavier Fernandes

Abstract

The electrification of transportation requires cost-effective energy storage systems with high energy densities. Aprotic sodium-oxygen batteries offer great promise for advanced energy storage as these batteries possess lower charge overpotential and higher reversibility, when compared to their lithium-oxygen battery cousins. To bring aprotic sodium-oxygen batteries closer to commercialization, a deeper understanding into the underlying cell chemistry and its limitations is required.

In this thesis, phase-transfer catalysis is shown to be responsible for the growth and dissolution of cubic sodium superoxide crystals and the reversible cell capacity. In the absence of phase-transfer catalysis, quasi-amorphous sodium superoxide films are formed, and cells exhibit negligible capacity. Similar effects were also observed in lithium-oxygen cells.

Following this result, direct evidence of solution-mediated superoxide transport in the sodium-oxygen cell is revealed. Using ESR spectroscopy coupled with parallel SEM studies, hydroperoxyl (HO_2) radicals were successfully spin-trapped via reaction with 5,5-Dimethyl-pyrroline N-oxide at different electrochemical stages, allowing monitoring of superoxide production and consumption during cycling. On discharge, the variation of superoxide content in the electrolyte, and its correlation with the crystallization of cubic sodium superoxide agrees with the classical LaMer mechanism of nucleation and growth. On charge, the oxidation of sodium

superoxide, through reverse solution processes, reduces the superoxide content in the electrolyte and lowers the charge overpotential. Interestingly, the addition of H_2O in the electrolyte significantly increases the concentration of soluble superoxide. Furthermore, carbon-centered/oxygen-centered alkyl radical intermediates are identified, and they arise from the attack of HO_2 intermediates on the diglyme solvent.

Finally, the growth of sodium dendrites on the anode and the electrochemically inert by-products that passivate the cathode are revealed as the primary causes for early cell termination of sodium-oxygen batteries.

The research presented here leads to a new understanding into the aprotic sodium-oxygen chemistry that, significantly, extends to lithium-oxygen batteries and explains their different behaviour.

Acknowledgements

First and foremost, I would like to thank my two supervisors Linda Nazar and Graham Murphy. I am very thankful and appreciative of their guidance and encouragement. I extend my thanks to them for their support, which allowed my projects to progress smoothly. I would like to also thank my committee members Dr. Vivek Maheshwari and Dr. Michael Pope for their presence and support.

I would like to extend a special thanks to Dr. Chun Xia. Chun Xia is an unparalleled researcher, and I am honoured to have had the opportunity to work, learn, and discuss with him. I thank him for all the time, guidance, and words of wisdom he has given me.

I would like to also thank my parents, Romualdo and Maria, my brother Ronson, and my sister Vanessa for providing me support and unconditional love. I would like to thank my co-workers Robert Black and Brian Adams. I would lastly like to thank the following people, from the University of Waterloo Writing Center, that helped me in editing my thesis: Mandy Penney, Janne Janke, and John Vardon.

Table of Contents

List of Figures

List of Tables

1 Introduction

Due to the desires to minimize CO_2 emissions, the market for alternative green energy storage and conversion systems is rapidly expanding. It is reported that internal combustion engine (ICE) vehicles annually produce 4500 kg of CO_2/ vehicle with the assumption of a 20000 km vehicle mileage.[1] Canada's total greenhouse gas (GHG) emissions between 1990 and 2014 were 120 megatonnes of carbon dioxide equivalent, 32 % of which were attributed to automotive transportation.[2] Consequently, research into electric vehicles (EVs) has been gaining pronounced momentum, as it is well understood that the electrification of transportation by "green" energy sources (e.g., sunlight and wind) would minimize the consumption of fossil fuels and, thereby, reduce CO_2 emissions. EVs utilize electric motors for propulsion and are only powered by electrical energy. Furthermore, the energy conversion efficiencies of EVs are much greater than those of ICE vehicles. EVs convert approximately 90 % of their input energy into turning their wheels, while ICE vehicles convert approximately 12.6 %.[3] The EVs in the market today are mainly powered by secondary batteries (also known as rechargeable batteries). Through charge and discharge, electrical energy is reversibly stored and released from the battery; on discharge, the electrical energy powers EVs' propulsion systems. Presently, battery powered EVs are unable to achieve the target driving range of 800 km as they are limited by the low practical energy densities of current battery technologies.[3] EVs' success therefore depends on developing advanced cost-effective batteries with high energy densities. In 2012 the main battery suppliers, e.g., Nissan, Tesla, and Mitsubishi, disclosed total revenues hitting 83.5 billion USD. These revenues are predicted to reach 271.67 billion USD in 2019.[4] Accordingly, from an industrial stand point, the EV market is a very lucrative business.

1.1 Overview of Li-ion Batteries

Today, the most widely used rechargeable battery is the lithium-ion battery (LIB). First established commercially by Sony in 1991, LIBs are now implemented in most consumer electronic devices (e.g., mobile phones) and EVs.[5,6]

As shown in **Figure 1.1**, a typical LIB contains a lithium graphite anode, a lithium containing transition metal oxide cathode (e.g., $LiCoO_2$), and an ion conducting electrolyte. LIBs function through intercalation and deintercalation mechanisms. On charge, lithium ions from the lithium containing transition metal oxide cathode react with electrons and are intercalated into the layered carbon anode. On discharge, lithium ions are deintercalated from the layered carbon anode, react with electrons, and are intercalated into the lithium deficient transition metal oxide cathode.[7,8]

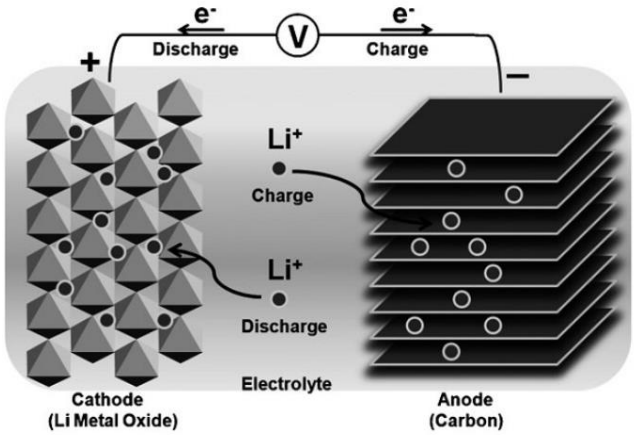

Anodic Reaction:

$$xLiC_6 \rightleftharpoons xC_6 + xLi^+ + xe^-$$

Cathodic Reaction:

$$Li_{1-x}CoO_2 + xLi^+ + xe^- \rightleftharpoons LiCoO_2$$

Overall Reaction:

$$xLiC_6 + Li_{1-x}CoO_2 \rightleftharpoons LiCoO_2 + xC_6$$

Figure 1.1 Working principle of a typical lithium-ion battery.[5,9]

The advantages of LIBs are limited by their energy density and high cost.[10] As previously mentioned, the target driving range is 800 km per charge or, in terms of battery energy, 125 kWh per charge. Current LIBs are capable of delivering capacities of approximately 200 Wh kg^{-1} ($LiCoO_2$); therefore, to meet the 800 km driving range, 600 kg of $LiCoO_2$ electrode material is required.[3] The electrode material is expensive and significantly increases the cost of the battery. For example, the cost of a Tesla Model 3 battery pack is $260 per kWh.[11] It is therefore not surprising that the Tesla Model S 90D, which possesses the largest driving range (~470 km) today, costs $89500 USD (base model).[12] The cost of current EVs makes them unable to compete with conventional vehicles equipped with ICEs. As a result, an ideal electric vehicle that is modestly priced (< $40000 USD) and can travel over 800 km on one charge may be out of this technology's reach. Moving beyond the LIB is a formidable challenge and will require the exploration of novel battery chemistries with higher energy densities and lower cost.[13]

1.2 Non-Aqueous Alkali Metal-Oxygen Batteries

In the search for advanced rechargeable batteries that are viable for automotive transportation, research has turned to alkali metal-air batteries, e.g., lithium-air and sodium-air batteries,[3] which are considered the most attractive alternatives to LIBs, when high energy density is a critical requirement. In comparison to LIBs, alkali metal-air batteries allow for a three- to four-fold increase in practical energy density.

The lithium-air battery, also known as the lithium-oxygen cell (Li-O_2 cell), is a promising metal-oxygen electrochemical redox couple that is widely researched due to its superior theoretical

energy density. The theoretical energy density of Li-O_2 cells is approximately 3505 Wh kg^{-1} (Li_2O_2), which is the highest among the other rechargeable systems.[14]

A very similar system to the lithium-air battery is the non-aqueous sodium-air battery, also known as the sodium-oxygen cell (Na-O_2 cell), which possesses a theoretical energy density of 1105 Wh kg^{-1} (NaO_2). Janek's seminal study on the rechargeable Na-O_2 cell demonstrated the better electrochemical reversibility of the Na-O_2 system in comparison to that of the Li-O_2 system.[15] As a result, the Na-O_2 cell has recently emerged as a promising battery technology.[16]

1.2.1 Principles of Non-Aqueous Li-O_2 and Na-O_2 Batteries

The non-aqueous aprotic Li-O_2 cell contains a lithium anode, an oxygen permeable cathode, and an organic electrolyte that provides a conductive medium for the lithium ions to move between the electrodes.[17]

On discharge, the process where oxidation occurs at the anode and electrons are passed to the cathode for reduction, oxygen reacts with lithium ions, in the presence of electrons, forming lithium peroxide, Li_2O_2, which is stored within the voids of the oxygen permeable cathode. On charge, the process where oxidation occurs at the cathode and electrons are passed to the anode for reduction, the Li_2O_2 is reversibly oxidized to lithium ions and oxygen, while the lithium ions re-deposit as lithium on the anode.[18] The working principles are illustrated in **Figure 1.2**.

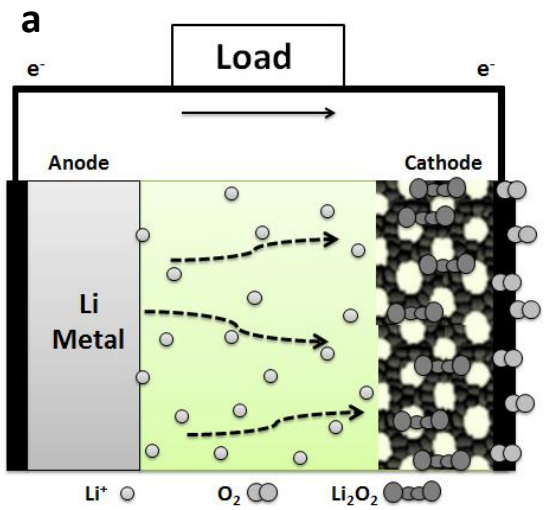

b

Anodic Reaction:

$$2Li \rightleftharpoons 2Li^+ + 2e^-$$

Cathodic Reaction:

$$2Li^+ + O_2 + 2e^- \rightleftharpoons Li_2O_2$$

Overall Reaction:

$$2Li + O_2 \rightleftharpoons Li_2O_2$$

Figure 1.2 (**a**) Systematic illustration of the lithium-air battery on discharge. The reverse occurs on charge. (**b**) Electrochemical reactions involved in a lithium-air battery, where discharge proceeds to the right and charge proceeds to the left.

Analogous to the Li-O_2 cell, the Na-O_2 cell contains a sodium anode, an oxygen permeable cathode, and a sodium ion conducting organic electrolyte. On discharge, oxygen reacts with sodium ions, in the presence of electrons, forming sodium superoxide, NaO_2, which is stored within the voids of the oxygen permeable cathode. On charge, the NaO_2 is reversibly oxidized to sodium ions and oxygen, while the sodium ions re-deposit as sodium on the anode. The working principles are illustrated in **Figure 1.3**.[15]

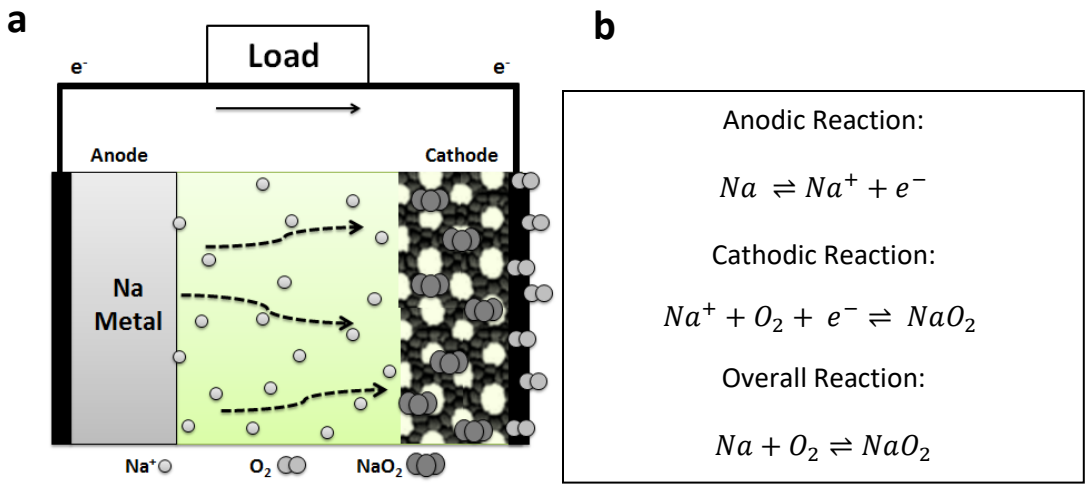

Figure 1.3 (**a**) Systematic illustration of the sodium-air battery on discharge. The reverse occurs on charge. (**b**) Electrochemical reactions involved in a sodium-air battery, where discharge proceeds to the right and charge proceeds to the left.

1.2.2 Characteristic Differences between Non-Aqueous Li-O_2 and Na-O_2 Batteries

Na-O_2 and Li-O_2 batteries have similar cell configurations; nonetheless, they possess many characteristic differences.[16]

Cathode Kinetics. The electrochemical reactivity of sodium and lithium towards oxygen is similar, in that initial reduction at the cathode forms the superoxide radical species, AO_2 (A = Na, Li); however, the difference is that sodium superoxide, NaO_2, is a stable compound, whereas lithium superoxide, LiO_2, is not.[19] The latter is thermodynamically unstable, although it has been trapped as an intermediate in Li-O_2 cells and identified using Raman and magnetic measurements.[20-22] Accordingly, LiO_2 intermediates are chemically (or electrochemically) converted to Li_2O_2 by a disproportionation reaction (or a second electrochemical reduction).[18] The chemical disproportionation mechanism involves a one-electron reaction followed by a chemical disproportionation of lithium superoxide, LiO_2, as shown in reactions R1 and R2.[20,23,24]

$$O_2 + Li^+ + e^- \rightarrow LiO_2 \qquad \text{R1}$$

$$2LiO_2 \rightarrow Li_2O_2 + O_2 \qquad \text{R2}$$

The electrochemical reduction mechanism involves two sequential electron transfer steps, as shown in reactions R3 and R4.[25,26]

$$O_2 + Li^+ + e^- \rightarrow LiO_2 \qquad \text{R3}$$

$$LiO_2 + Li^+ + e^- \rightarrow Li_2O_2 \qquad \text{R4}$$

On charge, the solid Li_2O_2 is oxidized to oxygen without first forming LiO_2; consequently, the discharge and charge reactions of the Li-O_2 battery do not follow the same paths. The charge reactions are shown in reactions R5 and R6.[27]

$$Li_2O_2 \rightarrow Li_{2-x}O_2 + xLi^+ + xe^- \qquad \text{R5}$$

$$Li_{2-x}O_2 \rightarrow O_2 + (2-x)Li^+ + (2-x)e^- \qquad \text{R6}$$

In contrast, NaO_2 – being a thermodynamically stable product – is observed in the Na-O_2 cell. NaO_2 is not, however, the only discharge product described in the literature. Various authors have reported the formation of sodium peroxide (Na_2O_2) on the cathode upon discharge, commonly crystallized with two water molecules ($Na_2O_2{\cdot}2H_2O$).[28,29,30,31] In an Na-O_2 cell, the formation of NaO_2 during discharge competes with Na_2O_2 due to their close thermodynamic equilibrium potentials (2.27 V vs. 2.33 V, respectively). These potentials are credited to their close Gibbs free energy of reaction, ΔG, as shown in reactions R7 and R8.[15]

$$2Na^+ + 2O_2 + 2e^- \rightarrow 2NaO_2 \qquad \Delta G = -437.5\ kJ\ mol(2NaO_2)^{-1} \qquad \text{R7}$$

$$2Na^+ + O_2 + 2e^- \rightarrow Na_2O_2 \qquad \Delta G = -449.7\ kJ\ mol(Na_2O_2)^{-1} \qquad \text{R8}$$

For completeness, the charge reactions of NaO_2 and Na_2O_2 are shown below in reactions R9 and R10, respectively.

$$NaO_2 \rightarrow Na^+ + O_2 + e^- \qquad \text{R9}$$

$$Na_2O_2 \rightarrow 2Na^+ + O_2 + 2e^- \qquad \text{R10}$$

Properties and Morphologies of Discharge Products. The discharge products observed in Li-O_2 and Na-O_2 cells are largely different, both in their properties and morphologies. In the Li-O_2 cell, the Li_2O_2 discharge products have been observed as toroid-shaped crystals with diameters of approximately 500 nm (**Figure 1.4a**).[32] In contrast, in the Na-O_2 cell, the NaO_2 discharge products have been observed as micron sized cubic crystals (**Figure 1.4b**).[15] Transmission electron microscopy (TEM) studies have demonstrated that Li_2O_2 toroids are aggregates composed of many Li_2O_2 nanocrystals[32], while NaO_2 cubes are speculated to grow as single crystals.[15] The discharge products in Li-O_2 and Na-O_2 cells also possess different electrochemical properties. The oxidation of Li_2O_2 typically requires overpotentials of 1 V.[27] Contrastingly, the oxidation of NaO_2 typically requires overpotentials of 0.2 V.[15] Overpotential, the potential difference between the experimentally observed potential and the equilibrium potential, is driven by kinetics. When cell overpotential is present, more energy is required for input into the system than for the energy output; therefore, overpotential results in an overall energy loss.

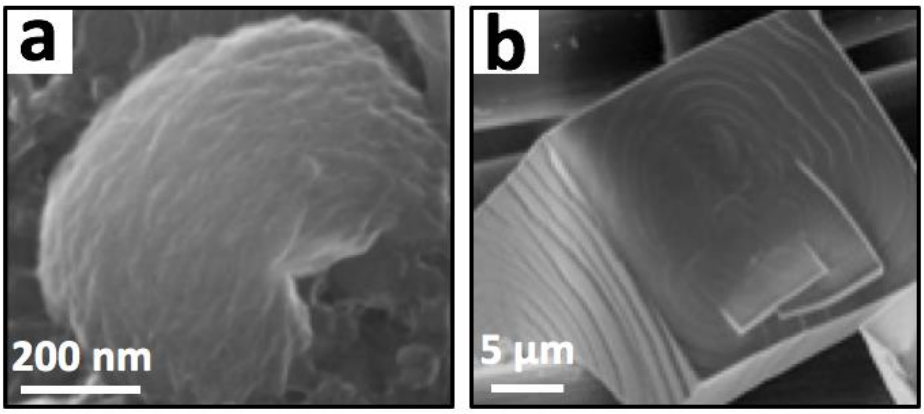

Figure 1.4 (**a**) SEM image of a toroidal Li_2O_2 discharge product formed at a current density of 10 µA cm^{-2} in a non-aqueous Li-O_2 cell.[32] (**b**) SEM image of a cubic NaO_2 discharge product formed at a current density of 200 µA cm^{-2} in a non-aqueous Na-O_2 cell.[19]

Electrochemical Behaviour. **Figure 1.5** compares the first discharge and charge curves of an Li-O_2 and an Na-O_2 cell. The open circuit potential of an Li-O_2 cell is 2.96 V (dashed line in **Figure 1.5a**).[33] Using an applied current of 20 µA cm^{-2}, a discharge plateau at 2.6 V is observed. This corresponds to a discharge overpotential of ~350 mV (η_{dis}). On charge, the overpotential dramatically increases, revealing a charge plateau at 4.2 V, which corresponds to a charge overpotential (η_{chg}) greater than 1 V. This overpotential is largely due to the insulating properties of Li_2O_2 products and by-products. Conversely, the Na-O_2 cell reveals an open circuit potential of 2.27 V (dashed line in **Figure 1.5b**) and low overall hysteresis ($\eta = \eta_{dis} + \eta_{chg}$) of approximately 200 mV at a current rate of 120 µA cm^{-2}.[15]

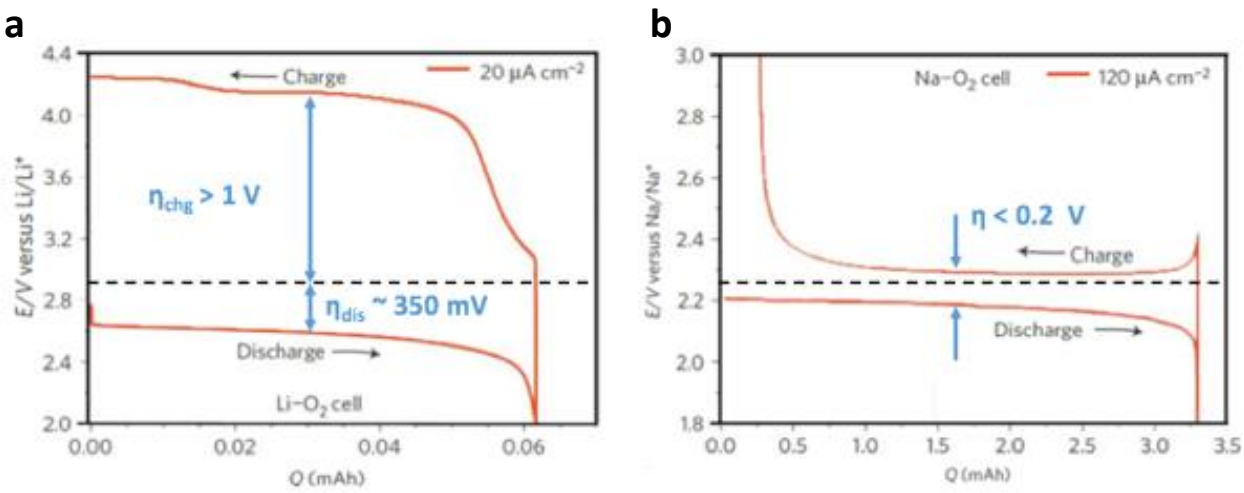

Figure 1.5 Discharge and charge curves of (**a**) an Li-O_2 cell and (**b**) an Na-O_2 cell.[15]

1.2.3 Main Challenges for Non-Aqueous Li-O_2 and Na-O_2 Batteries

Electrolyte Decomposition. Non-aqueous Li-O_2 and Na-O_2 batteries feature higher energy densities than current LIBs; however, the long-term cycling performance of Li-O_2 and Na-O_2 batteries is presently problematic.

Severe capacity fading, the decrease in reversible capacity during cycling, exists in Li-O_2 batteries.[32] In the Li-O_2 cell, capacity fading is attributed to the presence of the highly reactive superoxide radical as it is reported to react with and decompose many electrolytes, especially carbonate-based electrolytes.[34,35] Glyme-based, as opposed to carbonate-based, electrolytes have been reported to possess better stability against superoxide attack. Nevertheless, as shown in **Figure 1.6,** Bruce *et al.* demonstrated (using fourier transform infrared spectroscopy (FTIR) and differential electrochemical mass spectrometry (DEMS)) that glymes are also prone to superoxide attack.[36]

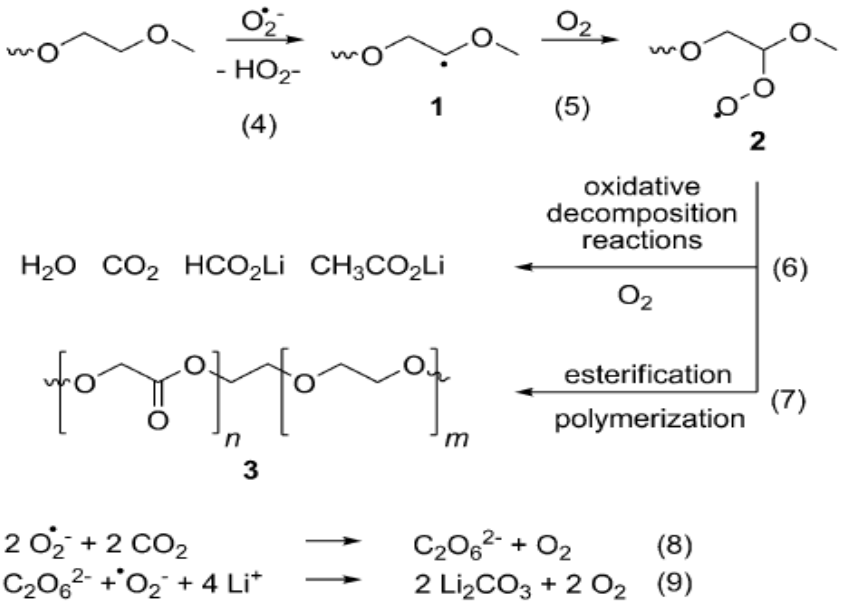

Figure 1.6 Mechanism of TEGDME decomposition on discharge in an Li-O_2 battery.[36]

As shown in **Figure 1.6,** the decomposition of glymes initiates through hydrogen abstraction and is followed by radical decomposition. Specifically, the superoxide radical is proposed to initiate hydrogen abstraction on a β carbon, methylene carbon, which results in a carbon-centered alkyl radical. These radicals are then believed to undergo oxidative decomposition reactions, analogous to combustion reactions, to form the observed glyme decomposition products.[36]

These electrolytes therefore lead to the formation of electrochemically inert species, such as lithium formate, lithium acetate, and lithium carbonate, on the porous carbon cathode. These insulating by-products passivate the cathode surface and result in the observed capacity fading.[37]

In the case of Na-O_2 batteries, despite the low overpotential and better chemical reversibility than those of Li-O_2 batteries, premature cell death upon cycling is also observed. Due to the similar nature of both cell chemistries, it is speculated that similar mechanisms of electrolyte decomposition by superoxide take place.[15] It has also been reported that carbonate-based electrolytes, such as propylene carbonate, result in the deposition of Na_2CO_3 by-products.[16]

Accordingly, opportunities exist in the research and development of electrolytes for both Li-O_2 and Na-O_2 cells.

Carbon Corrosion. In regards to the Li-O_2 battery, the IBM group concluded (based on DEMS results using isotopically labelled oxygen and carbon) that the carbon cathode is prone to chemical corrosion by Li_2O_2, which forms an insulating Li_2CO_3 layer (see R11 and R12).[37]

$$Li_2O_2 + C + \frac{1}{2} O_2 \rightarrow Li_2CO_3 \qquad \text{R11}$$

$$2Li_2O_2 + C \rightarrow Li_2CO_3 + Li_2O \qquad \text{R12}$$

Similarly, in Na-O_2 cells, corrosion of the carbon cathode by NaO_2 also exists and too restricts the long-term cell performance.[38] Accordingly, it is essential to explore cost-effective cathode materials with a high resistance to corrosion.

1.3 Motivations

Although much work has been carried out to develop advanced Li-O_2 and Na-O_2 batteries, many arguments over the underlying chemistry still remain. Here I list four open questions, which are the motivation for this work.

1.3.1 Mechanism of NaO_2 Growth: Surface-Conductive Pathway or Solution-Mediated Pathway?

On discharge of the Na-O_2 battery, NaO_2 products are deposited as micrometer-sized cubic crystals.[15] There has been much speculation on the mechanisms of NaO_2 crystal growth in the Na-O_2 battery and two pathways have been put forward.[19] These pathways are described below as a) and b).

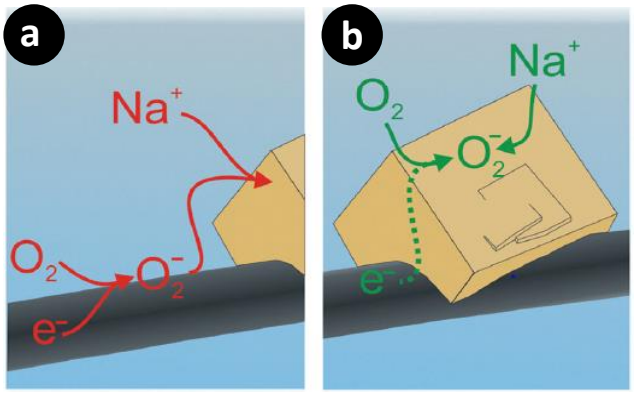

Figure 1.7 Schematic representation of the two possible growth mechanisms of NaO_2cubes, upon reduction of oxygen to the superoxide anion in the presence of sodium cations: (**a**) solution-mediated growth pathway and (**b**) surface-conductive growth pathway. [19]

a) Solution-Mediated Pathway: As shown in **Figure 1.7a**, the superoxide species dissolve in aprotic media and then transfer towards the surface of existing NaO_2 nuclei for further growth.[19] Shao-Horn and Lee concluded, based on their thermodynamic calculations, that superoxide exhibits much lower nucleation and dissolution energies than that of peroxide; accordingly, NaO_2 crystals may theoretically grow through solution-mediated processes.[39,40]

b) Surface-Conductive Pathway: As shown in **Figure 1.7b**, O_2 is reduced directly on the NaO_2 surface, and the resulting superoxide combines with Na^+ on existing NaO_2 nuclei for further growth.[19] Lee *et al.* concluded, based on their calculations, that the electronic and ionic conductivities of superoxide were higher than that of peroxide; accordingly, NaO_2 crystals may theoretically grow through surface-mediated processes.[39]

The growth mechanism of Na-O_2 batteries is of great interest as it would clarify the alkali sodium-oxygen chemistry that is widely sought by research groups worldwide.

1.3.2 Discharge Products of Na-O_2 Cells: NaO_2 or Na_2O_2?

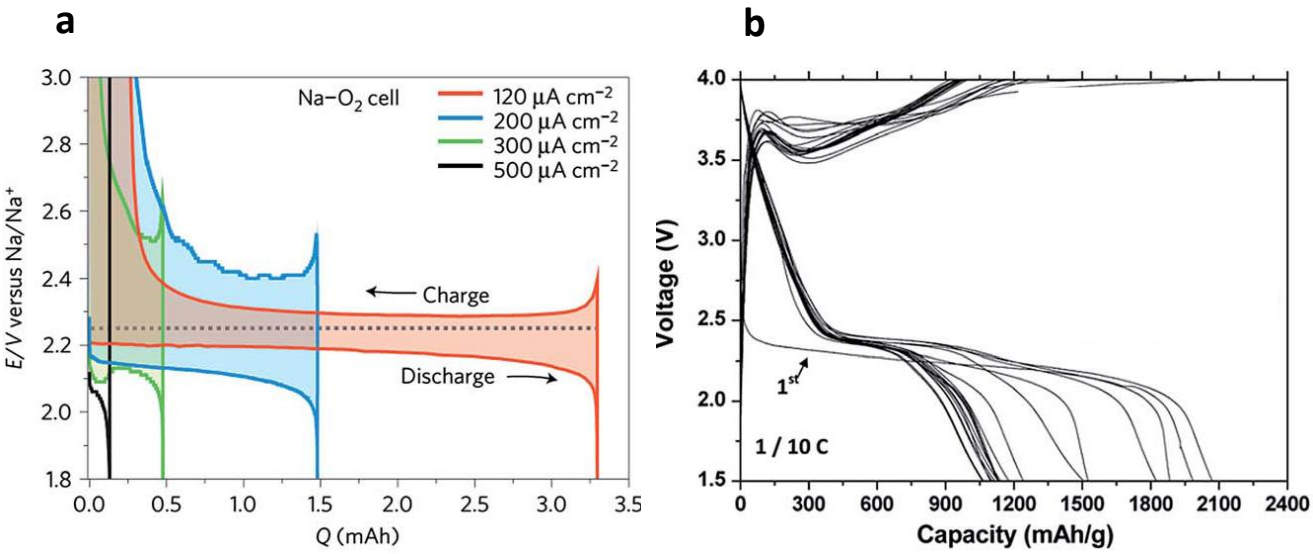

Figure 1.8 Discharge-charge cycles of Na-O_2 cells, where (**a**) NaO_2 is the main discharge product[15] and (**b**) Na_2O_2 is the main discharge product.[41]

Both NaO_2 and Na_2O_2 have been reported as the main discharge products of Na-O_2 cells. NaO_2 and Na_2O_2 present different electrochemical properties. As shown in **Figure 1.8**, NaO_2 presents a very low charge overpotential (typically below 200mV), while Na_2O_2 presents a high charge

overpotential, generally above 1 V, similar to Li_2O_2.[15,41] Accordingly, when the discharge product is NaO_2, the overpotential and instability of the cell are lower. Up till now, however, there is much controversy over the selectivity of discharge products in the Na-O_2 battery. Two opposing views are presented below in a) and b).

a) Thermodynamically Favoured Na_2O_2 A higher equilibrium potential exists for Na_2O_2 than that for NaO_2 (2.33 V vs. 2.27 V respectively). Na_2O_2 is therefore the thermodynamically preferred discharge product. Kang *et al.* concluded from their first principle calculations that Na_2O_2 is more stable as a bulk phase of sodium in an oxygen environment. However, they also reported that NaO_2 is more stable at the nanoscale.[42] Liu *et al.* observed that Na_2O_2 film products are formed on discharge, when DME-based electrolytes are used with graphene nanosheet cathodes.[31]

b) Kinetically Favoured NaO_2 The formation of NaO_2 requires a 1 e^- transfer in comparison to 2 e^- for Na_2O_2, which indicates that the former is kinetically preferred. Lee *et al.* predicted using DFT calculations that NaO_2 is the most stable phase at standard conditions of 300 K and 1 atm O_2.[43] In agreement with this prediction, Janek *et al.* observed the formation of cubic NaO_2 crystals at standard conditions, when diglyme-based electrolytes are used with GDL cathodes.[15]

Undoubtedly, understanding the conditions that favour the NaO_2 discharge product are of utmost significance, as they may enable researchers to improve the electrochemical performance of Na-O_2 cells.

1.3.3 Mechanism of Electrolyte Decomposition: Oxidative Cleavage Mechanism or H-Abstraction Mechanism?

Many problems in the Na-O_2 battery result from superoxide attack on electrolytes. Glyme-based electrolytes are reported to be more stable than those of alkyl carbonate-based electrolytes; however, glyme-based electrolytes also experience progressive decomposition upon cycling. Currently, there is much speculation on the mechanism of glyme based electrolyte decomposition, and two mechanisms are presented below in a) and b).

a) Peroxide-Induced Oxidative Cleavage Mechanism. Aurbach *et al.* claim that while superoxide is a "super"-nucleophile, it is a very poor radical. Accordingly, they speculate that the decomposition of glymes does not go through a radical-based mechanism. Instead, they propose that the decomposition of glymes goes through an oxidative cleavage mechanism via nucleophilic attack by Li_2O_2.[44]

b) Superoxide-Induced Hydrogen Abstraction Mechanism. Other groups suggest that the decomposition of glymes initiates through hydrogen abstraction and is followed by radical decomposition.[36]

Presently there is no experimental proof to validate either mechanism. Towards attaining a truly rechargeable battery, a stable electrolyte must be developed. Accordingly, a deeper understanding of how the reactive species interact with electrolytes is required. Hence, it is of great importance to determine the mechanism of electrolyte decomposition.

1.3.4 Primary Cause for the Failure of Na-O_2 Cells: Anodic Dendrite Growth or Cathodic Surface Passivation?

Outstanding cyclability has yet to be achieved in the Na-O_2 system. The two predominant failure mechanisms for cell termination are presented below in a) and b), both of which are operative.

a) Anodic Dendrite Growth. Many groups propose that the primary reason for the failure of Na-O_2 batteries is due to dendrite growth on the anode. During charge, sodium dendrites progressively permeate through the separator layer causing internal short circuits (**Figure 1.9a**). In accordance, Wu *et al.* employed a Nafion-Na^+ membrane as the electrolyte and suppressed the growth of sodium dendrites, which extended the lifetime of their Na-O_2 cells.[45] Recently Janek *et al.* reported that the replacement of sodium metal with sodiated carbon results in increased capacity and cell cycling performance. They also claim that the optimized anode restricted dendrite formation.[46]

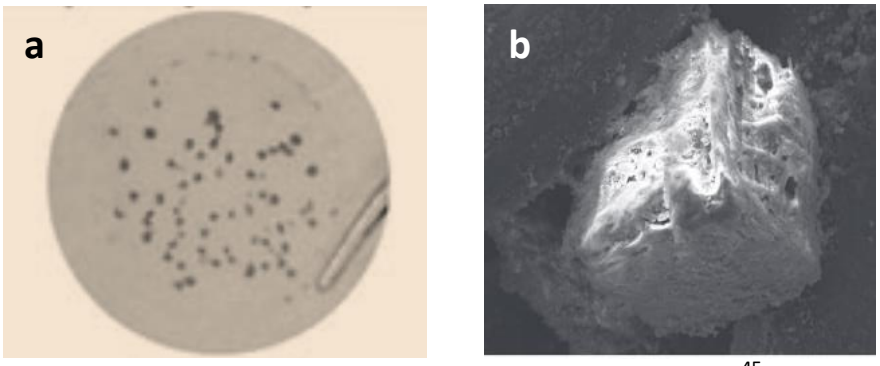

Figure 1.9 (**a**) Photograph of Na dendrites on a glass fiber separator.[45] (**b**) SEM image of a cathode after 10 cycles of discharge and charge.[19]

b) Cathodic Surface Passivation. Other groups concluded that cathode passivation is the main factor for the failure of Na-O_2 cells (**Figure 1.9b**). On the basis of NMR, DEMS, and iodometric titration studies, Black *et al.* recently demonstrated that the surface passivating layer is mainly composed of electrochemically inert formate, acetate, and carbonate, which originate from the decomposition of organic electrolyte. These side-products are not fully removed on charge; accordingly, the products accumulate in the cathode on cycling and in turn cause cell failure.[38]

A deeper understanding into the primary factors for cell failure is definitely needed. This understanding may allow researchers to tailor a high-performance Na-O_2 battery with outstanding cyclability.

1.4 Scope of Thesis

Chapter 1 is a general introduction presenting relevant research on the non-aqueous Li-O_2 and Na-O_2 batteries, and lists four of the main arguments regarding the underlying Na-O_2 chemistry. **Chapter 2** reveals the research methods and techniques used for this thesis. **Chapter 3** presents the critical role of proton phase transfer catalysis in Na-O_2 batteries. **Chapter 4** discloses direct evidence of solution-mediated superoxide transport and organic radical formation in Na-O_2 batteries. **Chapter 5** discusses the primary limitations on the rechargeability of Na-O_2 batteries. **Chapter 6** provides the future prospective for Na-O_2 batteries. **Chapter 7** comprehensively clarifies the arguments presented in **Chapter 1**, based on the results revealed in this thesis.

2 Experimental Methods and Theory

2.1 Chemicals and Materials

Here I list all chemicals and materials used in this thesis: diethylene glycol dimethyl ether (diglyme) (anhydrous, 99.5 %, Sigma-Aldrich), tetraethylene glycol dimethyl ether (99 %, Sigma-Aldrich), dimethyl sulfoxide (GC grade, > 99.5 %, Sigma-Aldrich), 5,5-dimethyl-1-pyrroline-N-oxide (GC grade, ≥ 98.0 %，Sigma-Aldrich), acetone (CHROMASOLV Plus, for HPLC, ≥ 99.9 %, Sigma-Aldrich), deuterium oxide (99.9 %, Sigma-Aldrich), benzoic acid (ACS reagent, ≥ 99.5 %, Sigma-Aldrich), glacial acetic acid (ACS reagent, ≥ 99.7 %, Sigma-Aldrich), sodium triflate (98 %, Sigma-Aldrich), sodium triflate (99.5 %, Solvionic), lithium triflate (99.995 %, Sigma-Aldrich), 1-butyl-1-methylpyrrolidinium bis(trifluoromethanesulfonyl)imide (99.9 %, Solvionic), sodium carbonate (BioXtra ≥ 99.0 %, Sigma-Aldrich), copper (II) trifluoromethanesulfonate (98 %, Sigma-Aldrich), bis(trifluoromethane) sulfonimide lithium salt (99.95 %, Sigma-Aldrich), sodium (I) bis(trifluoromethanesulfonyl)imide (99.5 %, Solvionic), potassium superoxide (Sigma-Aldrich), 18-crown-6 (99 %, Sigma-Aldrich), calcium hydride (reagent grade, 95 %, Sigma-Aldrich), oxygen (99.999 %, Praxair), sodium (ACS reagent, Sigma-Aldrich), lithium (foil ribbon, 0.75 mm thickness, 99.9 %, Sigma-Aldrich), molecular sieves (4 Å, beads 8-12 mesh, Sigma-Aldrich), stainless steel mesh (100 mesh, 316 grade), glass fiber separator (0.7 mm, Whatman), glass microfiber filter (GF/A 70 mm, Whatman), porous gas diffusion layer cathode (GDL H2315, Freudenberg), capillary tube (4 mm thin wall precision quartz, Wilmad-LabGlass).

2.2 Purification and Synthesis Techniques

Purification Techniques. Diethylene glycol dimethyl ether (diglyme) was distilled over calcium hydride under an N_2 atmosphere and stored over molecular sieves for one week prior to being used. DMSO was distilled over calcium hydride under reduced pressure and stored over molecular sieves for one week prior to being used. Benzoic acid was dried in a vacuum oven at 100^{o}C for 24 h, and glacial acetic acid was dried over molecular sieves for one week prior to being used. Sodium triflate (NaOTf, 98 %, Sigma-Aldrich) and lithium triflate (LiOTf, 99.995 %, Sigma-Aldrich) were vacuum-dried at 150 ^{o}C overnight using a Buchi glass oven and used for the research reported in **Chapter 3**. Sodium triflate (NaOTf, 99.5 %, Solvionic) was vacuum-dried at 150 ^{o}C overnight using a Buchi glass oven and used for the research reported in **Chapter 4** and **5**.

Synthesis of Sodium Trifluoromethanesulfonate (Sodium Triflate). To prepare pure sodium triflate (pure NaOTf), a solution of 3.32 g of sodium carbonate in 20 mL of distilled water was added drop wise over 40 min to a solution of 10.30 g of copper (II) trifluoromethanesulfonate in 80 mL of distilled water under an N_2 atmosphere. The solution was stirred for 12 h at room temperature and filtered three times by gravity using glass microfiber filters to remove the copper (II) carbonate, which is insoluble in water. The filtrate was evaporated under vacuum and heated until dry white precipitate was obtained. The precipitate was then dissolved in 300 mL of acetone. The solution was filtered three times by gravity using glass microfiber filters to remove the sodium carbonate, which is insoluble in acetone. The filtrate was evaporated under

vacuum and heated until dry white NaOTf powder was obtained. The NaOTf powder was finally dried in a vacuum oven at 150 °C overnight prior to being used.

2.3 Preparation of Solutions

Preparation of the Electrolyte Solutions. The NaOTf salt electrolyte solution was prepared in an argon-filled glove box (< 0.5 ppm H_2O and < 1.0 ppm O_2) with 0.5 M NaOTf in diglyme. The LiOTf salt electrolyte solution was prepared in an argon-filled glove box with 0.5 M LiOTf in diglyme. Different amounts of distilled water were added to the electrolytes, when required. The precise water content of the solutions was determined by Karl Fischer Titration.

Different amounts of acid (i.e., benzoic acid and glacial acetic acid) were added to NaOTf salt electrolyte solutions to give the desired proton concentrations. The solutions were prepared in an argon-filled glove box.

Preparation of Spin Trap Solution. The spin trap solution consisted of 0.1 M 5, 5-dimethyl-1-pyrroline-N-oxide (DMPO) in dimethyl sulfoxide (DMSO) and was prepared in an argon-filled glove box. DMPO was used as received, and DMSO was distilled as mentioned in Section 2.2.

2.4 Electrochemical Methods

2.4.1 Electrochemical Cells

Two-Electrode System. Non aqueous Li-O_2 and Na-O_2 cells were prepared using a modified Swagelok^{TM} design. These cells were assembled in an argon-filled glovebox using a porous gas diffusion layer cathode, a glass fiber separator, and a lithium or sodium anode. Both cathodes and separators were dried overnight at 300 ^{o}C under vacuum prior to being used. An electrolyte (50-200 µL) was added to the separator during cell assembly. The cell and its oxygen reservoir were sealed with 1.5 atm oxygen. All cells were rested at open circuit conditions for 2 h prior to measurements.

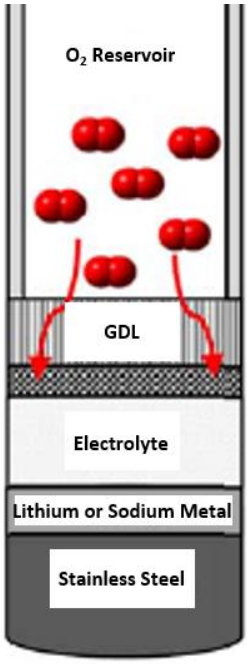

Figure 2.1 A schematic illustration of the two-electrode system.

Bulk Cell System. The bulk cell was assembled in an argon-filled glovebox. The cell was composed of a 20 mL glass vial (the vessel for the cell) and a modified rubber stopper. The modified rubber stopper consisted of a 1 mL syringe and two stainless steel wires with alligator clips soldered to the bottom of the wires. The gas diffusion layer cathode and sodium anode were clamped by the alligator clips to ensure good electrical contact. The needle of the syringe was installed into the rubber stopper, and its tip was approximately 1 mm from the GDL, which allowed for effective collection of soluble reaction intermediates and products. Prior to measurements, the glass vial was filled with 4.5 mL of electrolyte, plugged with the modified rubber stopper, transferred into an oxygen-filled glove bag (AtmosBag, Sigma-Aldrich), and purged with high purity oxygen. Both cathodes and separators were dried overnight at 300 ^{o}C under vacuum prior to being used.

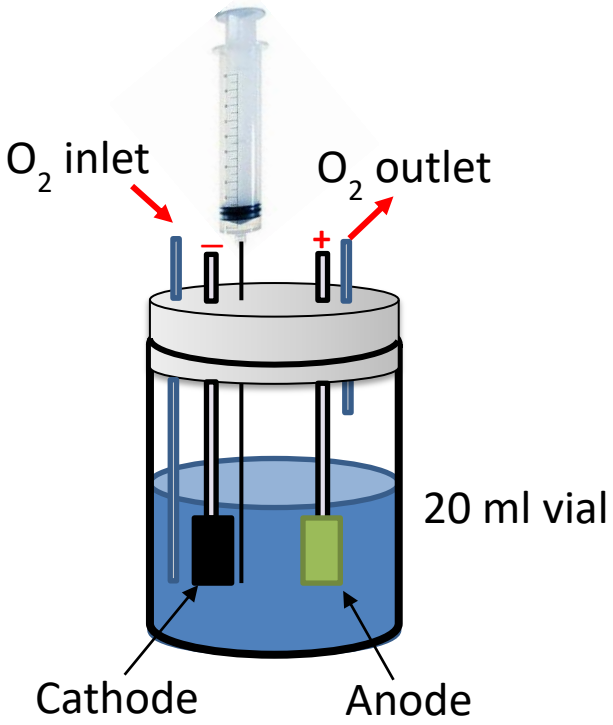

Figure 2.2 A schematic illustration of the bulk cell system.

2.4.2 Galvanostatic Cycling

Galvanostatic cycling is an electrochemical technique where current is applied and voltage is measured. In typical galvanostatic measurements, a constant current is applied to the cell until a preset cut-off voltage is reached, and then the current is reversed. The data obtained from this technique is commonly plotted with voltage on the y-axis and capacity on the x-axis.

All experiments were conducted on an Arbin BT-2000 multi-channel potentiostat. Unless otherwise stated, a constant current of 50 μA cm^{-2} was applied for both discharge and charge with cut-off voltages of 1.8 V and 4.5 V, respectively. Pristine GDL cathodes were used for discharge studies, while cathodes pre-discharged to 2 mAh cm^{-2} were used for charge studies. The electrochemical measurements for the two electrode systems were carried out under ambient conditions as the Swagelok™ two-electrode systems were gastight. The electrochemical measurements for the bulk cell systems were carried out in a N_2-filled glove bag.

2.4.3 Rotating (Ring) Disk Electrode

The rotating ring-disk electrode (RRDE) is a double working electrode, which functions in an environment of forced convection. The electrode rotates, inducing a vortex flow in the bulk electrolyte, and by convection drives analyte to the center and across the disk electrode. Convection increases transport of the analyte to the electrode; accordingly, the rotation of the ring disk electrode leads to higher currents, greater sensitivity, and reproducibility.[47]

The RRDE discussion that follows only applies to **Chapter 3** of this thesis, and all RRDE work was conducted with the help of Brian Adams. The experiments were controlled on two separate channels with a VMP3 potentiostat and EC-Lab® software (Bio-Logic Science Instruments). A glassy carbon disk and platinum ring RRDE tip set to a mechanical rotation of 200 rpm were used for these experiments (E7R9 RRDE tip, Pine Instruments, Co.). All tests were performed in an argon-filled glovebox with a gas-flow four-electrode cell setup. Metallic sodium strips were used as the counter and reference electrodes, and the RRDE was used as the two working electrodes. The electrolyte used was argon-purged or oxygen-saturated 0.1 M NaOTf in diglyme, with and without 500 ppm of distilled H_2O. In both cases, the synthesized NaOTf salt was used for the electrolyte. For the dry electrolyte, the H_2O content was < 1 ppm before and after conducting the electrochemical experiments. For the experiments with the electrolyte containing 500 ppm of H_2O, the counter electrode was a Pt wire, and the reference electrode was a sodium strip in dry electrolyte, which was separated from the bulk electrolyte with a porous Vycor™ glass frit. The experimental collection efficiency ($N = I_{ring}/I_{disk}$) of the RRDE tip was calculated to be 42.4 % using the ferrocene/ferrocenium (Fc/Fc^+) redox couple in acetonitrile (3 mM Fc + 0.1 M tetrabutylammoniumhexafluorophosphate). The ring currents reported in this thesis were normalized to this value.

In **Chapter 3** of this thesis, the analyte was the superoxide intermediate. Accordingly, O_2 was reduced at the disk electrode by applying a cathodic potential sweep ($O_2 + e^- \rightarrow O_2^-$), and the reduced soluble species were forced to the ring electrode. The reduced species were detected

by their oxidation ($O_2^- \rightarrow O_2 + e^-$) at the ring electrode. The ring potential was held at 3 V vs. Na/Na^+.

2.5 Characterization Techniques

2.5.1 Scanning Electron Microscopy

The scanning electron microscope (SEM) is an imaging tool that provides information on the morphology of a sample and produces images by scanning a sample with a focused beam of electrons. The electrons interact with the sample and produce secondary electrons, backscattered electrons, and characteristic X-rays.

Secondary electron imaging is the standard detection mode and provides high-resolution imaging because secondary electrons are emitted very close to the sample surface. The focused beam of electrons, from the SEM, ejects secondary electrons, from the k-shell of the sample, by inelastic scattering interactions. The brightness of the computed image depends on the number of secondary electrons reaching the detector. Secondary electron imaging is able to produce an image resolution of 0.5 nm or less.[48]

Backscattered electrons are reflected from the sample by elastic scattering. These electrons emerge from deeper locations within the sample; consequently, the resolution of backscattered electron imaging is generally poorer than that of secondary electron imaging. However, the intensity of backscattered electrons may be much greater than that of secondary electrons as the intensity of backscattered electrons is related to atomic number. Accordingly, heavier

elements appear brighter than those of lighter elements. Therefore, backscattered electron imaging allows for contrast among areas with different chemical compositions.[48]

A characteristic X-ray is emitted when the electron beam, from the SEM, ejects an electron from an inner shell of the sample, and, simultaneously, a higher-energy electron from an outer shell fills the inner shell vacancy. The X-ray produced is characteristic of an element. SEMs' equipped for energy-dispersive X-ray (EDX) spectroscopy allow for the detection of X-rays. These X-rays may be used to map the distribution and estimate the abundance of elements.[48]

The secondary electron detector was used for all images, and, when required, EDX spectroscopy was used in parallel. SEM samples were prepared in an argon-filled glove box. The samples were transferred to the SEM under anaerobic conditions.

All samples were investigated using a LEO 1530 field-emission SEM equipped with an EDX spectroscope attachment (Zeiss).

2.5.2 X-Ray Diffraction

X-ray diffraction is used to identify the atomic and molecular structure of a crystal through the diffraction of incident X-rays by atoms. The atoms' electrons scatter the X-ray waves; accordingly, secondary spherical waves result. These resulting waves usually cancel out in most directions through destructive interference; however, they do add constructively in a few specific directions and are determined by Bragg's law:[49]

$$n \cdot \lambda = 2 \cdot dsin\theta$$

In this equation n is an integer, λ is the wavelength of the beam, d is the spacing between the diffracting planes, and θ is the incident angle.

The principles of X-ray diffraction are illustrated in **Figure 2.3**. Two parallel incident X-rays labeled A and B are diffracted by atoms in the sample; however, X-ray B must travel 2·dsinθ further than X-ray A. Should the two diffracted X-rays be in phase and of a multiple of the X-ray wavelength, n·λ, then the distance between the crystal planes, d, may be obtained by scanning over various incident angles, θ. X-ray diffraction patterns, being unique to crystalline samples, are used for sample identification.[49]

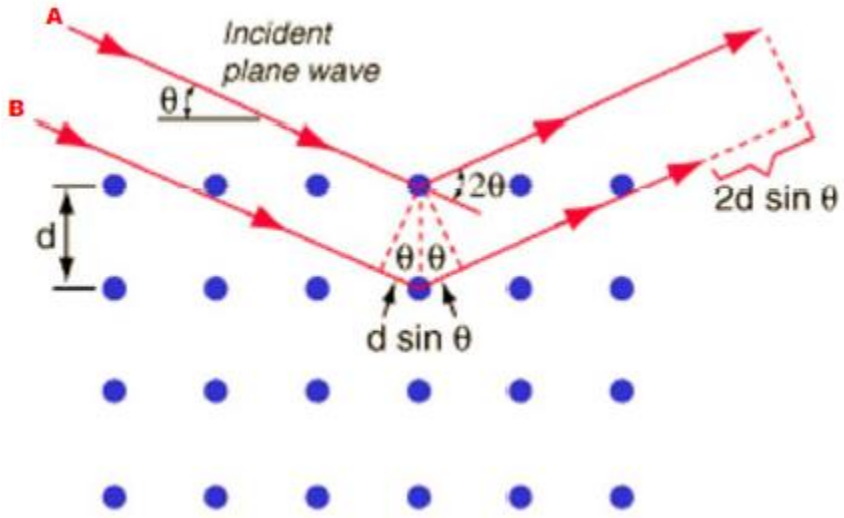

Figure 2.3 A schematic illustration of X-ray diffraction.

All XRD patterns were collected using a Bruker D8-Advance (Cu-$K_{\alpha 1}$ radiation; λ = 1.5405 Å). The XRD patterns were performed in air using a gastight sample holder. All samples were prepared in an argon-filled glove box.

2.5.3 ^{1}H Nuclear Magnetic Resonance Spectroscopy

Nuclear magnetic resonance (NMR) spectroscopy exploits the magnetic properties of certain atomic nuclei. NMR spectroscopy is commonly used to investigate the physical and chemical properties of organic molecules.

In ^{1}H NMR spectroscopy the external magnetic field causes electrons in the sample to resonate, thus generating local magnetic fields that oppose the external field. These sample-induced local magnetic fields shield proton nuclei; accordingly, for the proton nuclei to achieve resonance (absorption of electromagnetic radiation at a characteristic frequency of the isotope), the external magnetic field must be increased. This variation in the external magnetic field produces a signal on the frequency scale, which is designated as the NMR signal.[50]

All NMR experiments were conducted at room temperature on a 300 MHz Bruker Advance NMR Spectrometer. The deuterated solvent used was D_2O, and, therefore, all ^{1}H NMR spectra were referenced to its residual solvent peak at 4.78 ppm. The samples were prepared in an argon-filled glove box. All sample solutions contained 100 µL of sample and 600 µL of D_2O. For the analysis of by-products in **Chapter 4**, the cathodes were immersed in 700 µL of D_2O for 30 min, and the resting solutions were directly analyzed.

2.5.4 Electron Spin Resonance Spectroscopy

Electron spin resonance (ESR) spectroscopy is used to study samples with unpaired electrons. It is particularly useful for studying metal complexes or organic radicals. Its principles are similar to that of NMR; however, ESR monitors the magnetic field strength required to achieve electron resonance.

The ESR discussion that follows only applies to **Chapter 4** of this thesis. All ESR measurements were conducted by the Baugh research group, and the preparation of the samples for analyses was conducted by the Nazar research group. For each ESR measurement, 100 µL of electrolyte was extracted from the Na-O_2 bulk cell system through the needle of the syringe without interruption to the ongoing electrochemical reactions. The extracted electrolyte was then mixed with 500 µL of 0.1 M DMPO/DMSO solution for 10 s. 100 µL of the resulting solution was immediately transferred into a capillary tube and sealed with a glass-gas inlet stopper for a continuous-wave (CW) ESR measurement at 210K.

CW ESR spectra were collected using a Bruker X-band EMXmicro equipped with EMX standard resonator and ESR900 continuous flow cryostat (Oxford Instruments) for temperature control. Typical conditions of the ESR experiments were as follows: microwave frequency of 9.39 GHz, incident microwave power of 0.63 mW, and modulation field strength of 1 G with averaging 32 scans or 2 G with averaging 16 scans. Unless noted otherwise, ESR measurements were taken at 210 K.

3 The Critical Role of Phase Transfer Catalysis in Aprotic Na-O_2 Batteries

3.1 Introduction

In glyme-based electrolytes, solid NaO_2 is deposited as micron-sized cubic crystals that are quasi-reversibly oxidized to O_2 at very low overpotential. There has been much speculation on the mechanism of cubic crystal growth and dissolution.[15] In this study, I, together with my colleagues: Chun Xia, Robert Black, Brian Adams, and Linda Nazar (Professor, University of Waterloo), reveal that the solution-mediated growth pathway is dominant. Moreover, the pathway is almost exclusively driven by the presence of a proton phase transfer catalyst (PPTC). The PPTC solubilizes and transports the superoxide into solution through the formation of the highly soluble HO_2 radical.[51] The proton can be derived from any source such as impure salt hydrates or trace H_2O from the system. Key to understanding PPTCs' involvement in the Na-O_2 battery was the synthesis of pure anhydrous sodium triflate (NaOTf) salt. The results that follow explain why high overpotential on charge is characteristic of Li-O_2 but not Na-O_2. These results lead us to a deeper understanding of alkali-metal oxygen electrochemistry.

3.2 Comparison of Lab-Synthesized NaOTf and Commercial NaOTf Salts

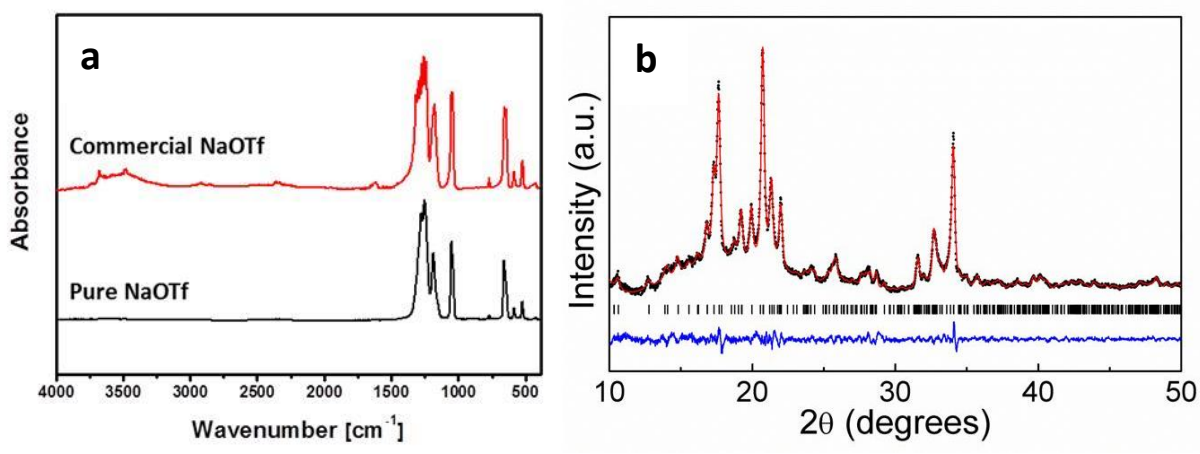

Figure 3.1 (**a**) Infrared spectra of commercial NaOTf (red) and pure (lab-synthesized) NaOTf (black) salts. (**b**) Powder X-ray diffraction pattern of the pure NaOTf salt at room temperature, and its Rietveld refinement. Shown are observed data (black dots), calculated data (red line), and the difference map (blue line) with reflection positions indicated by the black markers.

As shown in **Figure 3.1a**, the infrared spectra of the commercial NaOTf salt (98% purity, Aldrich) shows a strong absorption at ~3660 cm^{-1}, which is assigned to the stretching vibration of an OH group. Next to this sharp band, a broad absorption band between 3600-3000 cm^{-1} is observed and is assigned to water.[52] In the commercial synthesis of the NaOTf salt, NaOH is used as a reactant, and it tends to partially remain in the NaOTf salt.[53] NaOH is strongly hygroscopic and, therefore, can easily absorb water from air.[54] Other groups have attempted to purify the salt by filtering a NaOTf / ethanol solution; however, NaOH presents some solubility in ethanol (13.9 g / 100ml) and thus cannot be completely removed.[16] As a result, trace amounts of water are present in the commercial NaOTf salt, associated with NaOH, and result in relatively high water contents in the electrolyte (typically 10 ppm). In contrast, the NaOH hydrate is completely absent in the lab-synthesized NaOTf salt (pure NaOTf salt), which allows for the preparation of “pure” NaOTf salt electrolyte with very low water content (nominally “0 ppm”).

Figure 3.1b shows the XRD pattern and the Rietveld refinement of the pure NaOTf salt. The Rietveld refinement was carried out with DIFFRAC^{plus} TOPAS 4.2 using the fundamental parameters approach.[55] The structural model for the Rietveld refinement was adapted from Reference 56, which is a single crystal study of this compound.[56] The fit matches well, confirming the high purity of the compound. The lattice parameters are presented in Table 1 below and compared to those from Reference 56.

Table 3.1 XRD analysis of synthesized and literature NaOTf salts.

	This work	Ref. 56
a (Å)	9.803(2)	9.8130(2)
b (Å)	11.324(2)	11.3179(2)
c (Å)	11.574(2)	11.5910(2)
α (°)	102.108(8)	102.066(2)
β (°)	105.507(7)	105.634(2)
γ (°)	110.133(8)	110.205(2)
V (Å^3)	1095.8(3)	
χ^2	1.59	
R_p (%)	2.22	
R_{wp} (%)	3.05	

3.3 Effect of a Proton Phase Transfer Catalyst

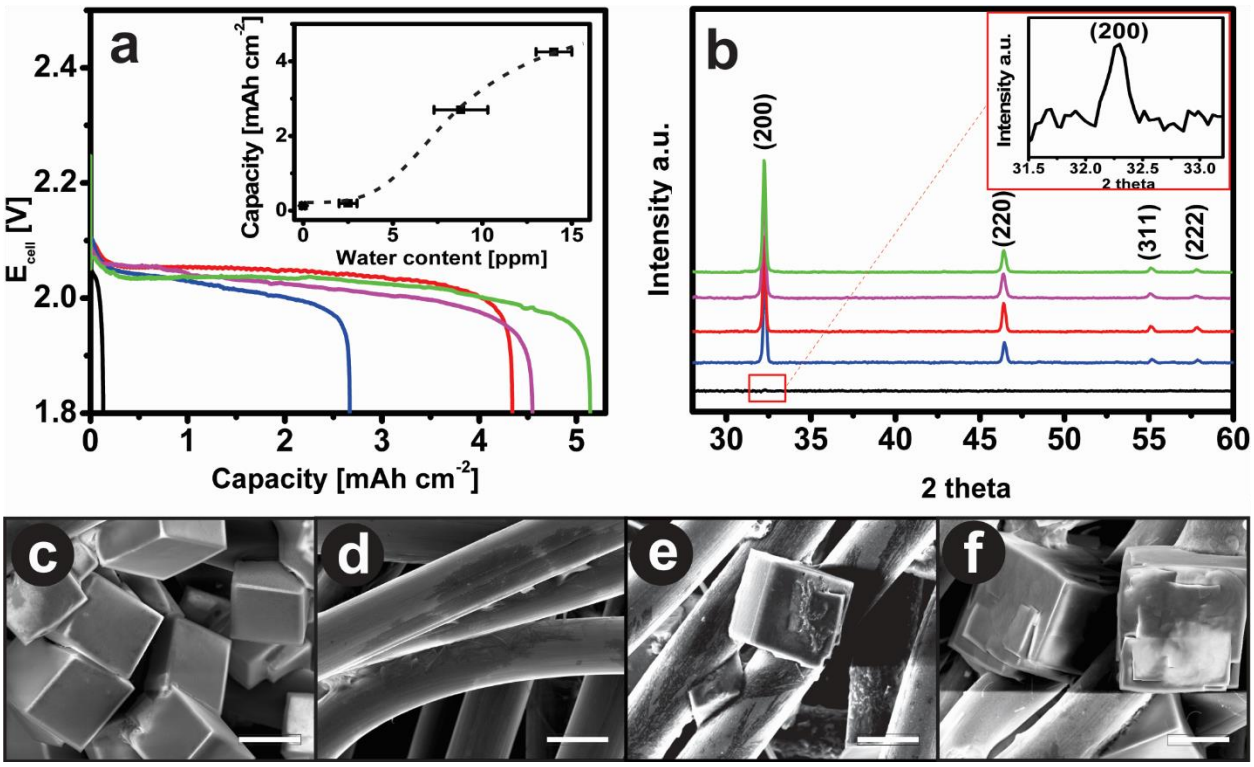

Figure 3.2 (**a**) First discharge curves of Na-O_2 cells using the pure NaOTf salt electrolyte with different concentrations of PPTCs at 50 µA cm^{-2}, with a cut-off voltage of 1.8 V, and (**b**) XRD patterns of the corresponding discharged cathodes: pure NaOTf (black), pure NaOTf with 8 ppm of H_2O (blue), pure NaOTf with 14 ppm of H_2O (red), pure NaOTf with 10 ppm of anhydrous benzoic acid (magenta), and pure NaOTf with 10 ppm of anhydrous acetic acid (green). The morphology of the discharge products using pure or commercial NaOTf salt electrolytes with or without PPTCs are shown in the SEM images: (**c**) pure NaOTf with 8 ppm of H_2O, (**d**) pure NaOTf, (**e**) commercial NaOTf, and (**f**) pure NaOTf with 10 ppm of anhydrous benzoic acid. Scale bars = 10 µm.

Figure 3.2 shows the effects of PPTCs on the ORR performance and discharge products. Commercial NaOTf salts displayed high discharge capacity at low overpotential and abundant coverage of the electrode surface with large crystalline NaO_2 cubes, as previously reported.[15]

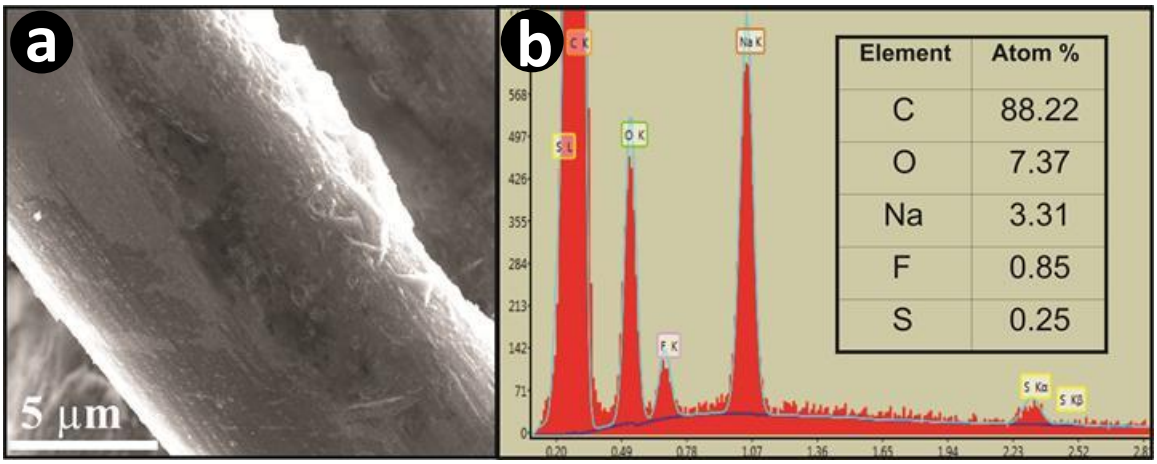

Figure 3.3 (**a**) SEM and (**b**) EDX data of the carbon gas diffusion layer electrode after full discharge using the pure NaOTf salt electrolyte.

In contrast, the pure NaOTf salt electrolyte, in the absence of a PPTC, behaved very differently. It yielded very low discharge capacity (*ca.* 0.1 mA cm^{-2}) at high overpotential (**Figure 3.2a**). SEM of the cathode, after full discharge using the pure NaOTf salt electrolyte, revealed no NaO_2 cubes; however, NaO_2 thin films were observed on the carbon fibers of the cathode (**Figure 3.2d** and **Figure 3.3a**). Energy-dispersive X-ray analysis of the film (**Figure 3.3b)** measured the expected 1:2 Na:O ratio of the product. The XRD signature of the (200) reflection of NaO_2 further confirmed NaO_2 formation (inset, **Figure 3.2b**).

The impurity in the commercial salt was NaOH and its associated water. This impurity leads to 10 (± 1) ppm of water in the electrolyte using 0.5 M commercial NaOTf salt, as determined by Karl-Fisher titration. Accordingly, adding a trace amount of water (8 ± 1 ppm) to the electrolyte with pure NaOTf salt results in a massive increase in discharge capacity to 2.65 mA cm^{-2} (**Figure 3.2a,** blue curve) and a plethora of ~10 µm crystalline NaO_2 cubes (**Figure 3.2c).** The discharge capacity and the dimension of NaO_2 cubes increase with higher water content. H_2O – but more

specifically the proton – is vitally involved in the catalytic crystal growth of NaO_2. Using trace amounts (~10 ppm) of anhydrous weak acids as the PPTC, e.g., benzoic acid (**Figure 3.2f**), the same effects were observed. In the Li-O_2 cell, high concentrations of H_2O (500 – 4000 ppm) have been reported to increase capacity via solvation of LiO_2.[57] In order to clarify the interaction of H_2O with superoxide and determine whether superoxide may follow the solvation mechanism instead of the PPTC mechanism, the following calculations were made. On discharge, oxygen is initially reduced to O_2^-: $O_2 + e \rightarrow O_2^-$. The rate of production, J, of O_2^- is calculated according to Faraday's law: $J = I/nF$. At the applied current of 0.1 mA, which was used for all cells, the rate of production of O_2^- is therefore:

$$J = 0.1 * 10^{-3}\ A \div\ (1 \times 96485\ C\ mol^{-1}) = 1.04 * 10^{-9}\ mol *\ s^{-1}$$

Thus, after one minute of discharge, 62 * 10^{-9} mol of superoxide would be generated. This amount can be compared to the quantity of PPTC available. A total of 20 µL of the pure NaOTf salt electrolyte, with 10 ppm of PPTC (e.g., H_2O, or HA), was added to the cathode during assembly. The density of the electrolyte is ~1 g mL^{-1}. Hence, the total number of moles of PPTC in the electrolyte, N, is therefore:

$$N_{\mathrm{H2O}} = \frac{20\ \mu l * 10^{-3} \times 1\ g\ ml^{-1}\ \times 10 * 10^{-6}}{18\ g\ mol^{-1}} = 11.11 * 10^{-9}\ mol$$

$$N_{\mathrm{benzoic\ acid}} = \frac{20\ \mu l * 10^{-3} \times 1\ g\ ml^{-1}\ \times 10 * 10^{-6}}{60\ g\ mol^{-1}} = 3.33 * 10^{-9}\ mol$$

Consequently, the total amount of superoxide produced within the first minute of cell operation exceeds the total amount of PPTC added by a factor of 5 – 40 fold. None of the PPTCs added are therefore capable of solvating the NaO_2 with a coordination sphere (even at 100

ppm), given this ratio. Thus "solvation" of the superoxide by water or weak acid can be ruled out.

3.4 Oxygen Evolution Activity

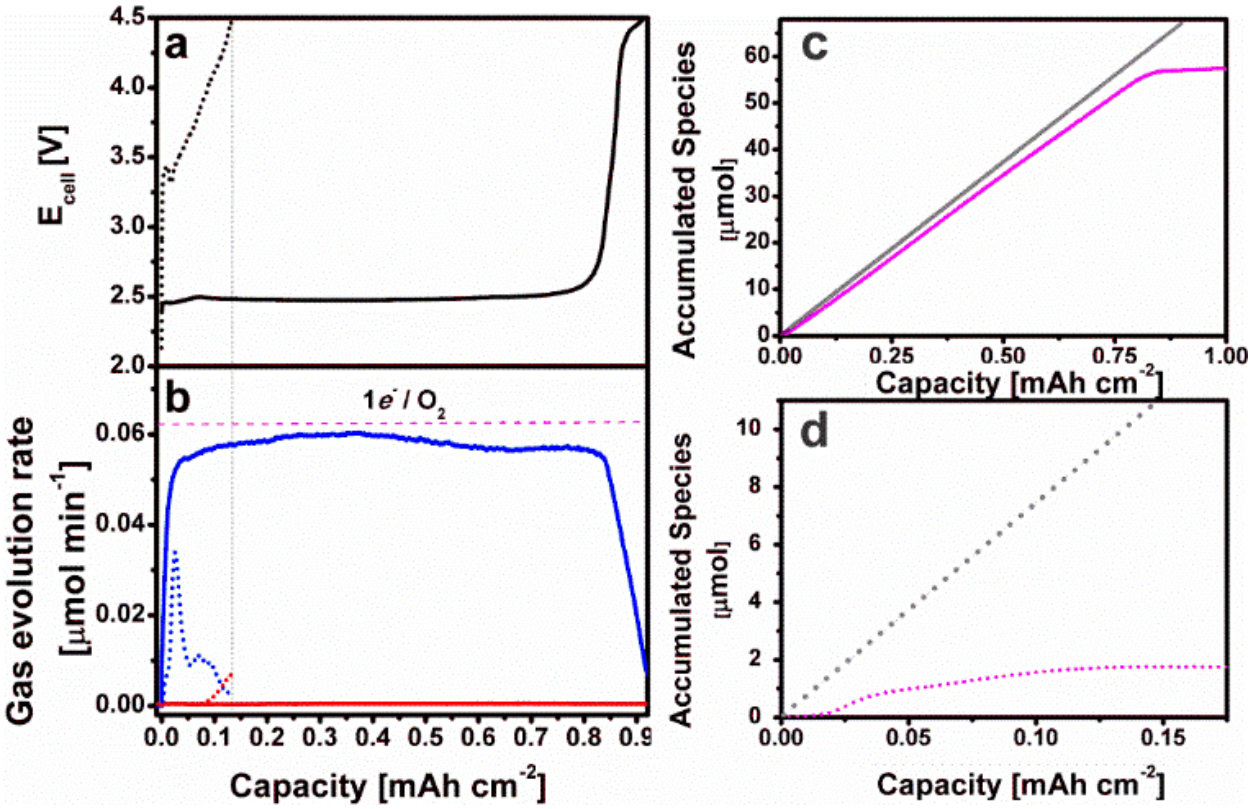

Figure 3.4 Oxygen evolution monitored by on-line mass spectrometry (OEMS). (**a**) Charge profiles of Na-O_2 cells using the pure NaOTf salt electrolyte (dotted line) and the pure NaOTf salt electrolyte with 8 ppm of H_2O (solid line) at 0.5 mA cm^{-2} with a cut-off voltage of 4.5 V, and (**b**) the corresponding gaseous products, O_2 (blue) and CO_2 (red), evolved during charge. (**c**) and (**d**) the accumulative evolved oxygen (magenta) and electron (gray) as a function of charge capacity on the basis of OEMS results presented in (**a**) and (**b**). Prior to charge, the cell using the pure NaOTf salt electrolyte was fully discharged to 1.8 V giving a low discharge capacity of 0.13 mAh cm^{-2}, while the cell using the pure NaOTf salt electrolyte with 10 ppm of H_2O was partially discharged to 1 mAh cm^{-2}.

Figure 3.4 shows the results of oxygen evolution from Na-O_2 cells measured by *in-situ* mass spectrometry. Comparison of the capacity on charge with the oxygen evolved using the pure

NaOTf salt electrolyte with 8 ppm of H_2O (**Figure 3.4a** and **b**) provides a charge ratio of 1.1 e^-/O_2 (**Figure 3.4c**). This charge ratio is nearly identical to that for a commercial NaOTf salt electrolyte.[16] The oxygen evolution profile (**Figure 3.4b**), corresponding to a flat voltage plateau, is constant throughout the state of charge. It is not accompanied by CO_2 evolution even up to 4.5 V, indicating that no significant carbonates are formed *via* side-reactions that could be oxidized on charge. This result contrasts with typical Li-O_2 cells, which show multiple stages of oxygen evolution and CO_2 evolution, indicative of complex reactions.[58] The behaviour is completely different for the pure NaOTf salt electrolyte without the addition of H_2O. Using the pure NaOTf salt electrolyte, the voltage profile dramatically slopes and exhibits a much larger overpotential (onset ~3.3 V). Oxygen evolution associated with the pure NaOTf salt electrolyte is extremely low when compared to that of the pure NaOTf salt electrolyte with the addition of H_2O. The oxygen evolution of the pure NaOTf salt electrolyte is not constant and primarily occurs at the onset of charge. At the end of charge, the e^-/O_2 ratio is ~5.75 e^-/O_2. This indicates that oxygen evolution is a highly kinetically hindered process in the absence of a PPTC. Charge using the pure NaOTf salt electrolyte is not surprisingly accompanied by significant side reactions. The evolution of CO_2 occurs above 4 V, the typical decomposition voltage of alkyl carbonates.[58] The film-structured NaO_2 in the pure NaOTf salt electrolyte cell is believed to react at the carbon electrode interface to form Na_2CO_3, due to the large interfacial area.[59]

3.5 Mechanism

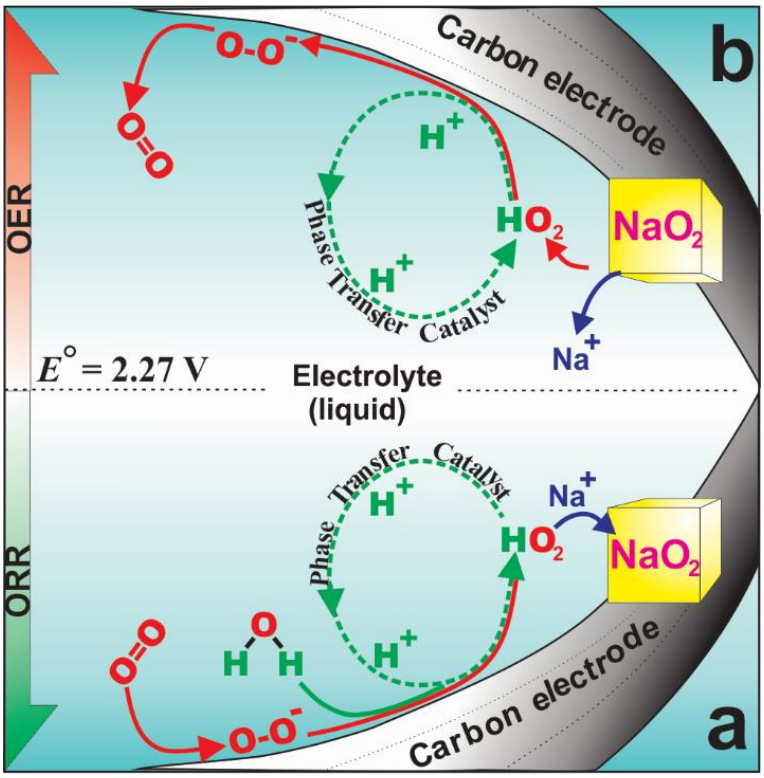

Figure 3.5 Schematic illustration of the mechanism of proton phase transfer catalysis. (**a**) ORR: oxygen is reduced at the surface to form superoxide, and superoxide reacts with trace H_2O to form soluble HO_2. The HO_2 undergoes metathesis with Na^+, driven by the free energy of formation of crystalline NaO_2, to form cubic nuclei that crystallize from solution. Growth of the NaO_2 from solution to form micron-sized cubes occurs via epitaxial growth promoted by phase transfer catalysis of the superoxide from solution to the solid. (**b**) OER is the reverse process: Protons in solution react with the surface of the NaO_2 cubes to generate HO_2, releasing Na^+ ions into the electrolyte. The soluble HO_2 is transported to the carbon surface, where it is oxidized to O_2.

The proton phase transfer catalysis mechanism is illustrated in **Figure 3.5**. Oxygen is initially reduced on the carbon surface forming superoxide (O_2^-). Reaction of surface-bound superoxide (O_2^-) with H_2O in solution yields HO_2 and OH^- ($O_2^- + H_2O \rightarrow HO_2 + OH^-$), based on the well-known property of superoxide as a strong Brønsted base.[60,61,62] In aprotic media, the above reaction dominates, when weak acids are present. HO_2, being a soluble intermediate, desorbs from the carbon surface, transfers into the electrolyte solution, and forms nuclei of NaO_2 *via*

metathesis on encounter with solvated Na^+ ions ($HO_2 + Na^+ \rightarrow NaO_2 + H^+$). This process thus regenerates the $H^+_{(solv)}$ catalyst for another cycle. Therefore, the proton acts as a carrier and continuously transports the superoxide from the electrode surface to solution. The following summarizes the reactions, with HA representing a weak acid:

$HA + O_2\bullet^- \leftrightarrows HO_2 + A^-$ (eq. 1)

$HO_2 + Na^+ \leftrightarrows NaO_2 + H^+$ (eq. 2)

Summary: $HA + O_2\bullet^- + Na^+ \rightarrow NaO_2 + A^- + H^+$

Overall: $O_2\bullet^- + Na^+ \rightarrow NaO_2$

The crystallization of NaO_2 strongly drives the equilibrium in eq. 1 to the right by the removal of HO_2 via eq. 2. This shift in the equilibrium of eq. 1 would make $O_2\bullet^-$ a stronger base than expected.[60,62] Once supersaturation of NaO_2 nuclei occurs, crystallization is thermodynamically favoured by the large free energy associated with formation of the NaO_2 lattice (ΔG = -437.5 kJ/mol).[42,63] In fact the peroxide, Na_2O_2, should be the thermodynamically favoured product, on the basis of its slightly lower free energy of formation (ΔG = - 449.7 kJ/mol). However, calculations notably reveal that these energies are reversed for nanocrystallites < 5 nm in dimension.[42] Accordingly, initial nucleation of nanodimensioned NaO_2 may elicit epitaxial growth and may be kinetically promoted by the PPTC. It is also important to note that HO_2 is aggressive towards organic electrolytes and oxygen rich surface functional groups, which result in the formation of side products (e.g., NaF and NaOAc) and limited cycling performance.[19] Thus only low quantities of PPTC can be tolerated in the cell.

3.6 Evidence of Solution-Mediated Processes

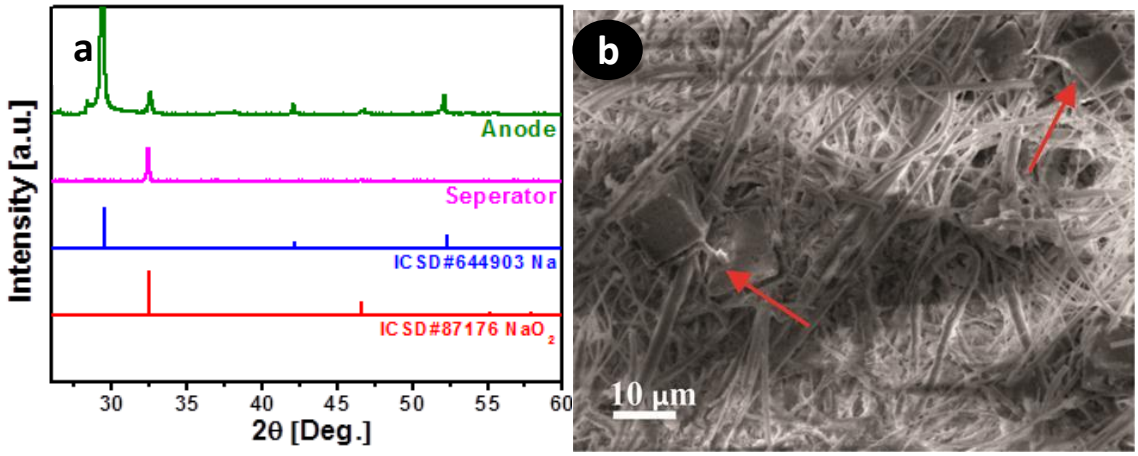

Figure 3.6 (**a**) XRD patterns of anode and glass fiber separator after full discharge to 1.8 V using the pure NaOTf salt electrolyte with 10 ppm of H_2O. (**b**) SEM image of corresponding glass fiber separator.

Figure 3.6a shows the XRD patterns of the separator and anode after full discharge using the pure NaOTf salt electrolytes with 10 ppm of H_2O. NaO_2 peaks appear in the patterns of both the separator and anode, indicating NaO_2 products are distributed across the entire Na-O_2 cell. In accordance, cubic NaO_2 crystals are observed on the glass fiber separator (**Figure 3.6b**). This evidence suggests that the irreversible diffusion of soluble HO_2 towards the separator and anode results in a small fraction of NaO_2 crystallizing on the separator and anode, which thereby lowers the charge efficiency.

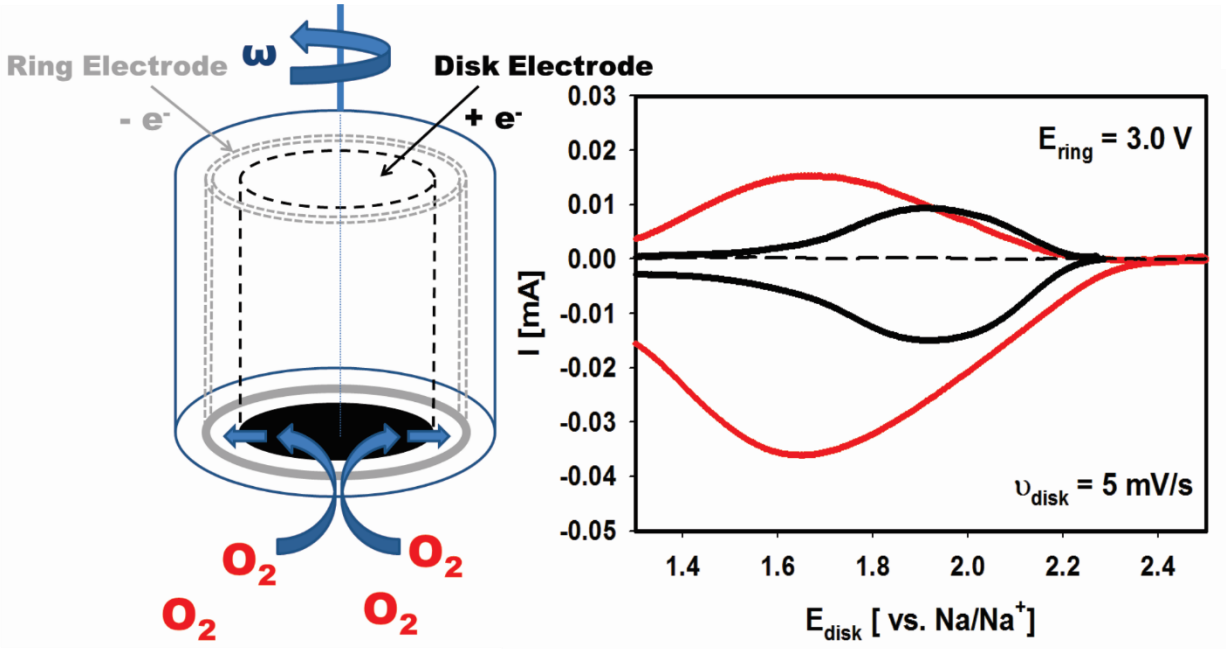

Figure 3.7 Rotating ring disk electrode (RRDE) analysis of superoxide transport in the pure NaOTf salt electrolyte, in the absence or presence of H_2O. A schematic diagram of the RRDE is displayed on the left. The RRDE tip used in this study consists of a glassy carbon disk and platinum ring imbedded into a PTFE rod with an insulating gap of PTFE between the two. Superoxide is generated at the glassy carbon disk and detected at the platinum ring at a rotation speed of 200 rpm. The addition of H_2O (red curve), compared to that without (black curve), provides a greatly enhanced current response, owing to superoxide transport in solution mediated by the PPTC. The dashed line is the ring current background under an argon atmosphere.

Figure 3.7 reveals concrete evidence for the solubilization of superoxide and its phase transfer reaction with water in the electrolyte. In the presence of H_2O, the linear sweep voltammogram reveals both a large disk current response, associated with the reduction of oxygen to superoxide, and a significant ring current response, associated with the oxidation of superoxide that was transported from the disk to the ring via solution. The onset of reduction in the presence of H_2O occurs 0.13 V higher than that of the reduction in the absence of H_2O, indicating a catalyzed process. More limited transport of NaO_2 results in the water-free electrolyte (~3-fold lower disk and ring currents). This accounts for the greatly reduced capacity

observed in full cells employing the pure NaOTf salt electrolyte without the addition of H_2O. Rapid passivation of the disk electrode commences at ~1.9 V (E_{disk}) for the pure NaOTf salt electrolyte. The pure NaOTf salt electrolyte containing the PPTC, H_2O, enhances the dissolution of O_2^-, freeing active sites on the glassy carbon disk electrode and, thereby, leads to a higher disk current with little passivation evident until ~1.6 V. Johnson *et al*. have also used the measure of ring:disk current in RRDE experiments to determine a partial solubility of LiO_2 in monoglyme. Our results for NaO_2 in anhydrous diglyme were similar to their findings. They further demonstrated a higher solubility of LiO_2 in DMSO using a gold disk electrode.[64] Solvation in DMSO is quite different from the phase-transfer process; yet, both processes result in higher capacity. Solvation does not however lower the overpotential on charge or discharge, whereas the PPTC lowers the overpotential for ORR as expected for a catalyzed process. More importantly, the PPTC significantly lowers the overpotential for OER.

3.7 Reversibility and Cycling

As illustrated in the proposed mechanism, the PPTC during charge must also reversibly transport the superoxide, *via* HO_2, from the NaO_2 crystallites to the surface of the carbon fiber cathode for oxidation (i.e., $NaO_2 + H^+_{(solv)} \rightarrow HO_2 + Na^+_{(solv)}$). The PPTC gives rise to the full charge capacity at a low overpotential, compared to negligible charge when the catalyst is absent. Since a very small amount of superoxide is deposited in the water-free Na-O_2 cell on discharge, it is difficult to prove whether the cell charges poorly due to reaction of superoxide with the carbon surface or a kinetically hindered process.

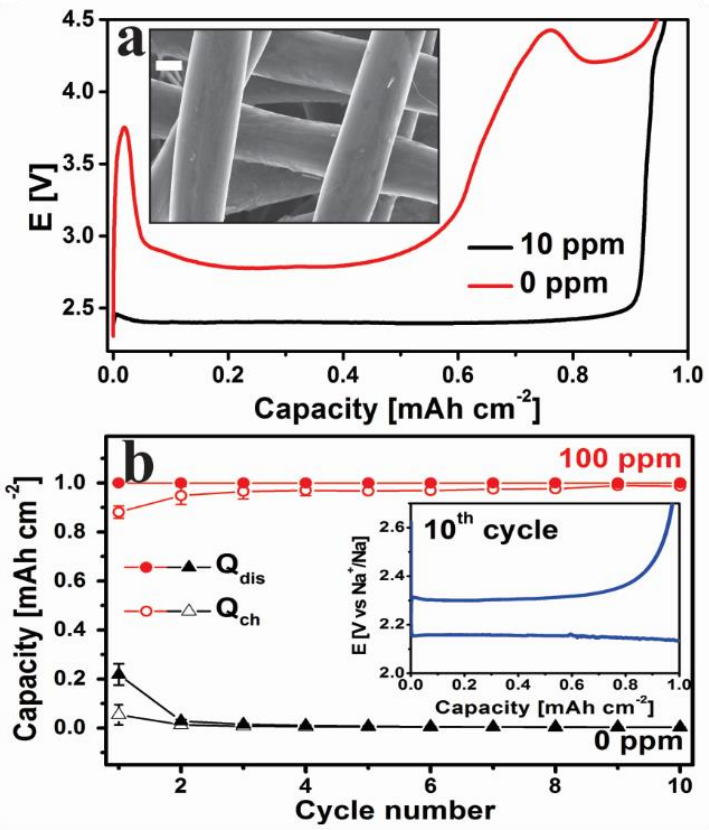

Figure 3.8 (**a**) The charge profiles of Na-O_2 cells using sodium anodes and cathodes pre-discharged to 1mAh cm^{-2} with the pure NaOTf salt electrolyte (black line) or the pure NaOTf salt electrolyte with 10 ppm of H_2O (red line). Cube-shaped NaO_2 can be oxidized only after charge up to 4.5 V using the pure NaOTf salt electrolyte without the addition of H_2O, as shown in the insert SEM image. (**b**) Cycling performance of Na-O_2 cells with a cut off capacity at 1mAh cm^{-2} using the pure NaOTf salt electrolyte (black triangles) or the pure NaOTf salt electrolyte with 10 ppm of H_2O (red circles). The insert shows the discharge and charge curves of the cell using the pure NaOTf salt electrolyte with 10 ppm of H_2O at the 10^{th} cycle.

Accordingly, to isolate charge from discharge, NaO_2 loaded electrodes were first prepared by discharging cathodes to 1 mAh in the pure NaOTf salt electrolyte containing 10 ppm of water. These cathodes were then extracted from the cell, thoroughly washed with anhydrous diglyme, and dried in a glove box. One set of electrodes was subjected to charge in the same electrolyte, and the other was charged in the pure NaOTf salt electrolyte without the addition of H_2O. **Figure 3.8** shows the results of the experiments. **Figure 3.8a** clearly reveals that the PPTC is critical for full oxidation of NaO_2 at low overpotential. The charging voltage (2.3 V) for the pure

NaOTf salt electrolyte with 10 ppm of H_2O is the same as previously reported for "dry" electrolytes. In the absence of the PPTC, a complex charge profile is observed. The apparent activation step at initial charge in the pure NaOTf salt electrolyte without the addition of H_2O is ascribed to electrolyte decomposition, which releases minute amounts of water. Gasteiger *et al*. reported a similar voltage jump for the oxidization of a cathode pre-filled with commercial Li_2O_2.[65] They suggested that, during the initial charge step, water is formed, and the water enabled the oxidation of Li_2O_2 via a solution process.

NaO_2 cubes are oxidized on full charge (see the insert SEM image in **Figure 3.8a**), although potentials in excess of 4.0 V are required in the absence of water, which would lead to extremely poor cycling in a normal voltage window. However, in the presence of the PPTC, 10 ppm of H_2O, cycling with over 95 % coulombic efficiency results **(Figure 3.8b**).

3.8 Effect of High Contents of PPTC

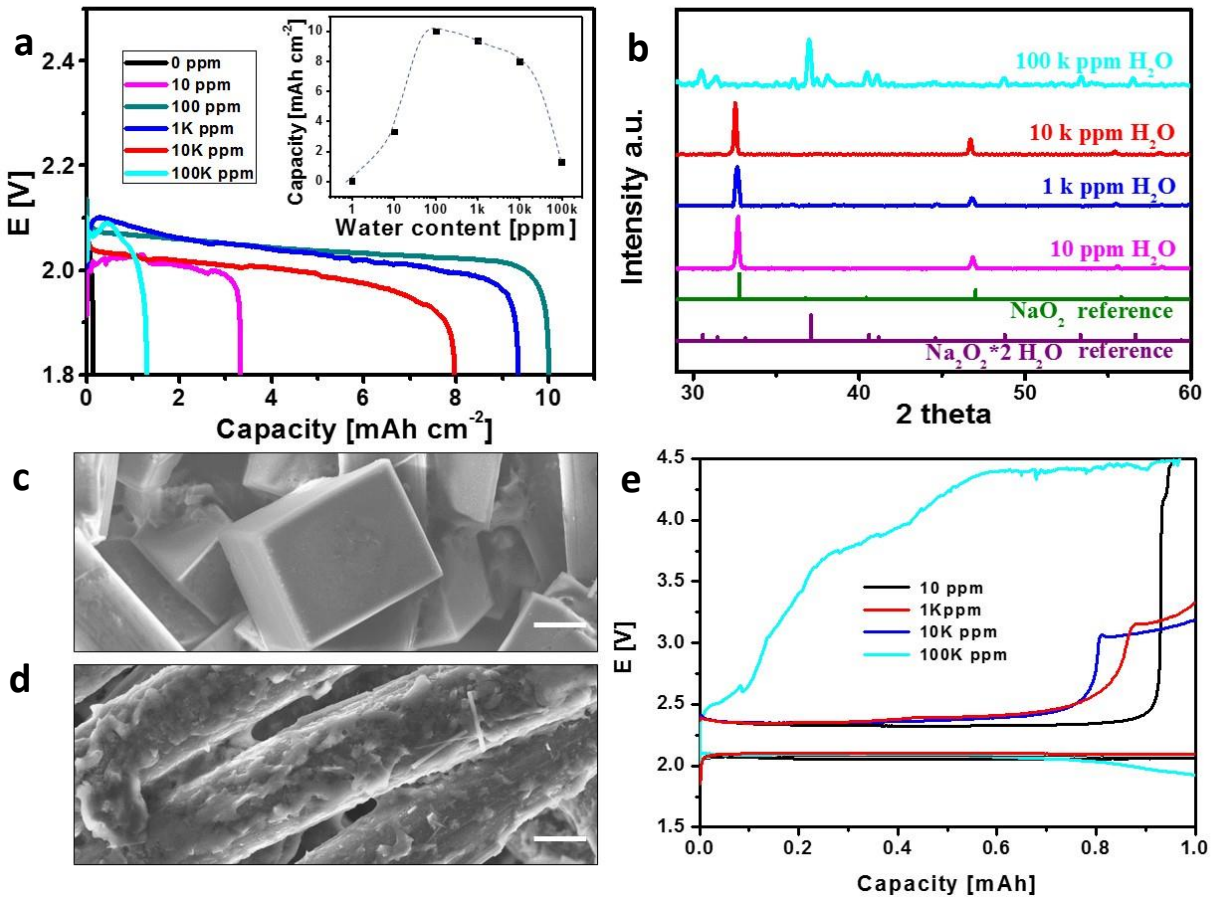

Figure 3.9 (**a**) First discharge curves of Na-O_2 cells using the pure NaOTf salt electrolyte with different concentrations of H_2O at 50 µA cm^{-2}, with a cut-off voltage of 1.8 V, and (**b**) XRD patterns of the corresponding discharged cathodes. The morphology of the discharge products using the pure NaOTf salt electrolyte with different concentrations of H_2O are shown in the SEM images: (**c**) 10 ppm of H_2O and (**d**) 100 K ppm of H_2O. (**e**) First charge curves of Na-O_2 cells using the pure NaOTf salt electrolyte with different concentrations of H_2O at 50 µA cm^{-2}, with a cut-off voltage of 4.5 V.

As shown in **Figure 3.9a**, the discharge capacity of an Na-O_2 cell with 100 ppm of H_2O in the pure NaOTf salt electrolyte is 10 mAh cm^{-2}. However, the discharge capacity rapidly drops to 1.5 mAh cm^{-2}, when the H_2O concentration is higher than 10 K ppm, signifying that other chemical processes are at work. **Figure 3.9b** shows XRD patterns of the cathodes that were discharged

with varying concentrations of H_2O. Below 10 K ppm of H_2O in the electrolyte, NaO_2 is identified as the main discharge product, while $Na_2O_2{\cdot}2H_2O$ is the main discharge product at high H_2O concentrations (~100 K ppm). The morphology of NaO_2 products are cube-shaped (**Figure 3.9c**), while $Na_2O_2{\cdot}2H_2O$ are film-like (**Figure 3.9d**). NaO_2 and $Na_2O_2{\cdot}2H_2O$ possess different electrochemical properties.[66] NaO_2 is oxidized at very low charge overpotential (< 0.2 V), while the oxidation of $Na_2O_2{\cdot}2H_2O$ presents a complex charge profile, i.e., a sloping-like charge curve below 4.2 V directly followed by a charge plateau at 4.4 V, similar to that of Li_2O_2.[41] The results clearly show that water content in the electrolyte plays an important role in the selectivity of the discharge products. Further studies into waters' effects on Na-O_2 batteries will be revealed in **Chapter 4**.

3.9 Effect of a PPTC in the Li-O_2 Cell

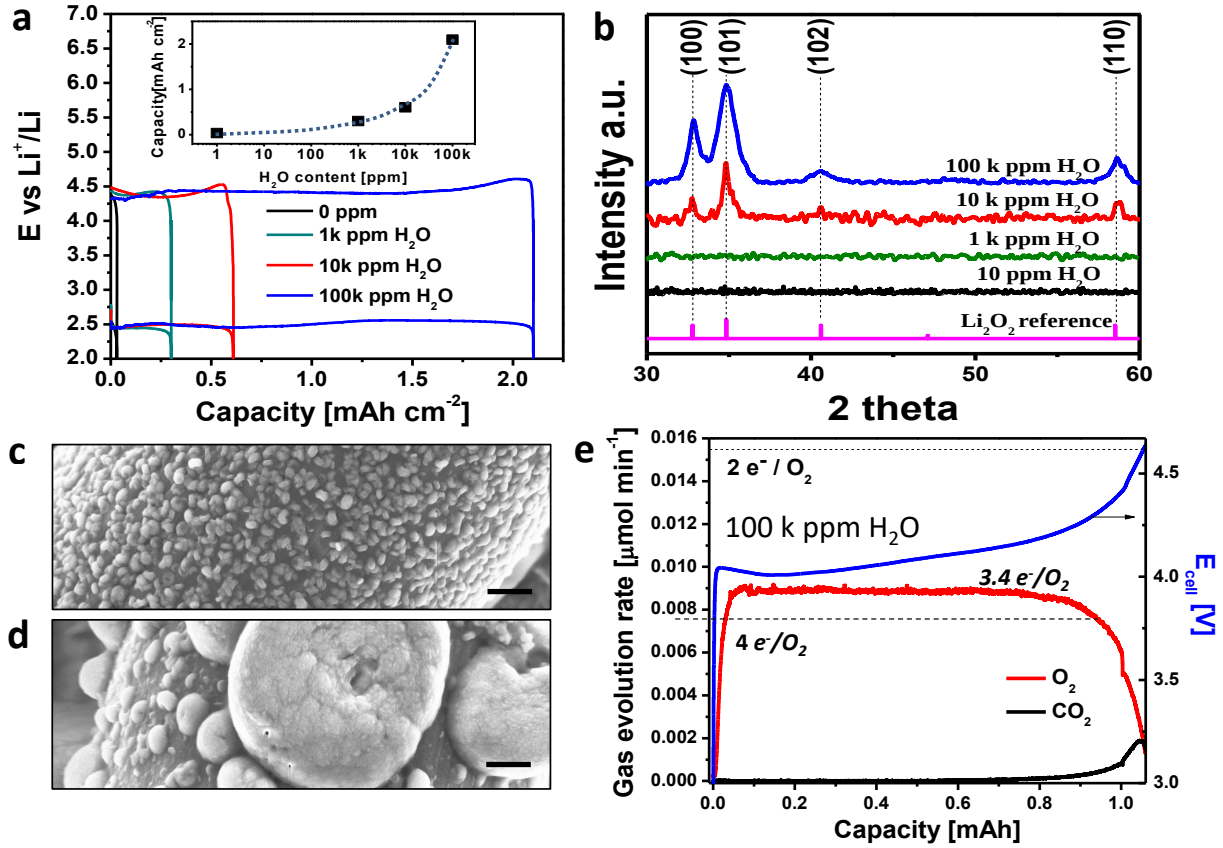

Figure 3.10 (**a**) First discharge-charge curves of Li-O_2 cells using LiOTf salt electrolyte with different concentrations of H_2O at 50 μA cm^{-2}, with a cut-off voltage of 2 V, and (**b**) XRD patterns of the corresponding discharged cathodes. The morphology of the discharge products using LiOTf salt electrolyte with different concentrations of H_2O are shown in the SEM images: (**c**) 1 K ppm of H_2O and (**d**) 100 K ppm of H_2O. (**e**) Charge profile of an Li-O_2 cell using LiOTf salt electrolyte with 100 K ppm of H_2O (blue) at 50 μA cm^{-2}, with a cut-off voltage of 5 V, and OEMS of its corresponding gaseous products, O_2 (red) and CO_2 (black), evolved during charge.

The Li-O_2 cell, similar to that of the Na-O_2 cell, is also expected to respond to PPTCs in the same manner. As shown in **Figure 3.10a**, the discharge capacity of Li-O_2 cells increases with increasing water content in the electrolyte. Different from Na-O_2 cells, H_2O does not distinctly influence the charge overpotential of Li-O_2 cells. XRD results of the carbon cathodes discharged with varying H_2O contents suggest that Li_2O_2 is the only crystalline discharge product (**Figure 3.10b**).

Moreover, the intensities of the Li_2O_2 diffraction peaks increase with increasing H_2O content, indicating that H_2O catalyzes the formation of Li_2O_2. Consistent with this conclusion, small Li_2O_2 particles with diameters of 200 nm are observed, when using an electrolyte with 1 K ppm of H_2O (**Figure 3.10c**). Large toroid-shaped Li_2O_2 particles with diameters of 1-5 μm are observed, when using an electrolyte with 100 K ppm of H_2O (**Figure 3.10d**). *On-line* mass spectrometry was used to investigate the gas evolution from an Li-O_2 cell, pre-discharged to 1 mAh cm^{-2}, using an electrolyte with 100 K ppm of H_2O. Similar to OEMS results of Na-O_2 cells, the oxygen evolution profile of the Li-O_2 cell is constant throughout the state of charge (**Figure 3.10e**). At the end of charge the e^-/O_2 ratio is calculated to be 3.4 e^-/O_2, which is much higher than the expected 2 e^-/O_2 for Li_2O_2 oxidation.[67] This indicates that the oxidation of Li_2O_2 is accompanied by significant side reactions. Gastiger *et al.* concluded from their ESR studies that singlet oxygen is formed upon Li_2O_2 oxidation.[68] Singlet oxygen, O_2 ($^1\Delta_g$), is a high energy form of oxygen and is extremely reactive towards organic electrolytes and carbon cathodes. Accordingly, the consumption of singlet oxygen by parasitic reactions may lead to less oxygen evolution during charge, as observed. The evolution of CO_2 is observed above 4.1 V and is the typical decomposition voltage of carbonates.[58] Both superoxide and singlet oxygen may trigger the decomposition of the electrolyte and the carbon cathode, leading to the observed carbonates. However, more studies are needed to further clarify the detailed kinetic processes involved on charge.

3.10 Conclusions

This study demonstrates the critical role of the PPTC in the Na-O_2 cell. In the presence of the PPTC, the transport of superoxide into the electrolyte is significantly enhanced through the formation of the soluble HO_2 intermediate. Accordingly, this intermediate initiates crystallization of NaO_2 in the solution phase rather than on the carbon surface. The catalyst-induced crystallization of cubic NaO_2 crystals is signalled by high discharge capacity at low overpotential. In the absence of the PPTC, crystalline NaO_2 thin films are observed with very low capacity. The active catalyst is the proton, H^+, and, therefore, any substance that can donate a proton to superoxide in aprotic media will function in this role. The presence of the PPTC also explains the growth of the less thermodynamically stable sodium superoxide as the PPTC provides a kinetic advantage to form micron-size crystallites. More importantly, the PPTC is vital to lowering the overpotential of the charge reaction. Although HO_2 is essential for significant cell capacity, its well-known reactivity will result in side reactions with the electrolyte and cathode support if concentrations are high.[57] Accordingly, future studies should be directed to exploring phase transfer catalysts with lower chemical reactivity.

This study also reveals the important difference from Li-O_2 cells. Gasteiger *et al*. reported that water enhances the solution transfer of Li_2O_2 to the carbon cathode surface for complete electrooxidation *via* the formation of a soluble H_2O_2 intermediate.[65] Interestingly, the addition of H_2O does not significantly affect the much higher charge overpotential ($\sim$1 V) of Li-O_2 cells, compared to that of Na-O_2 cells (< 0.2 V). This result may be due to several reasons. The formation of Li_2O_2 in Li-O_2 cells is accompanied by sluggish surface kinetics due to the formation

of stable side products (e.g., carbonate) in the discharge products, which maintain the high charge overpotential.[69] In contrast, Na-O_2 cells show a much higher yield of the desired NaO_2 and fewer parasitic reactions.[16] More importantly, in the presence of the PPTC (e.g., H_2O), the phase transfer from superoxide in solid NaO_2 is the catalysed reverse of the forward reaction to form NaO_2. However in the Li-O_2 cell, the initially formed LiO_2 is thermodynamically unstable. Disproportionation to form lithium peroxide thus favours the forward reaction at moderate current densities, where high capacities are observed. Therefore, the oxidation of peroxide goes through a different (uncatalysed, high energy) pathway as Nazar *et al.* have recently demonstrated,[27] and which has been predicted based on first principle calculations.[70] Similarly in Na-O_2 cells, when Na_2O_2 is the discharge product, these cells show poor reversibility and high overpotential.[28,71] This supports a concept that aprotic chemistry dominated by the formation of A_2O_2 (A = alkali) is inherently subject to high cell voltage on charge and poor round trip efficiency. As a result, future studies on the Li-O_2 cell, where Li_2O_2 is the main discharge product, should be directed to exploring suitable redox mediators. Alternatively, future developments in cell design and phase transfer catalysts offer very good prospects for a highly reversible Na-O_2 cell.

4 Direct Evidence of Solution-Mediated Superoxide Transport and Organic Radical Formation in Na-O_2 Batteries

4.1 Introduction

Although the effects of H_2O in both Li-O_2 and Na-O_2 cells are becoming better understood, direct evidence for the soluble hydroperoxyl radical was lacking prior to this study. In this study, I, together with my colleagues: Chun Xia, Franklin Cho, Niranjan Sudhakar, Brandon Buonacorsi, Sean Walker, Meng Xu, Jonathan Baugh (Associate Professor, University of Waterloo), and Linda Nazar (Professor, University of Waterloo), employed a unique combination of spectroscopic and microscopic techniques to elucidate this complex radical chemistry. This chapter quantifies the superoxide species in the electrolyte and on the solid cathode by using coupled electron spin resonance (ESR) spectroscopy and scanning electron microscopy (SEM) studies. ESR spectra and SEM images were collected in parallel and from *operando* cells as a function of charge passed and equilibration time. The results unequivocally demonstrate that the superoxide transfers through solution processes and leads to the formation and oxidation of NaO_2. On discharge, H_2O accelerates the solubilization of superoxide, which in turn leads to the crystallization of NaO_2 crystals from the electrolyte. Following the reverse path, superoxide is readily transported from the NaO_2 crystals to the cathode for oxidation. However, these solubilized superoxide species also attack the aprotic electrolyte, leading to the formation of organic radicals. This is the first *in-situ* evidence of organic radicals, which is important because they play a vital role in electrolyte degradation.

4.2 ESR Spin-Trap Technique

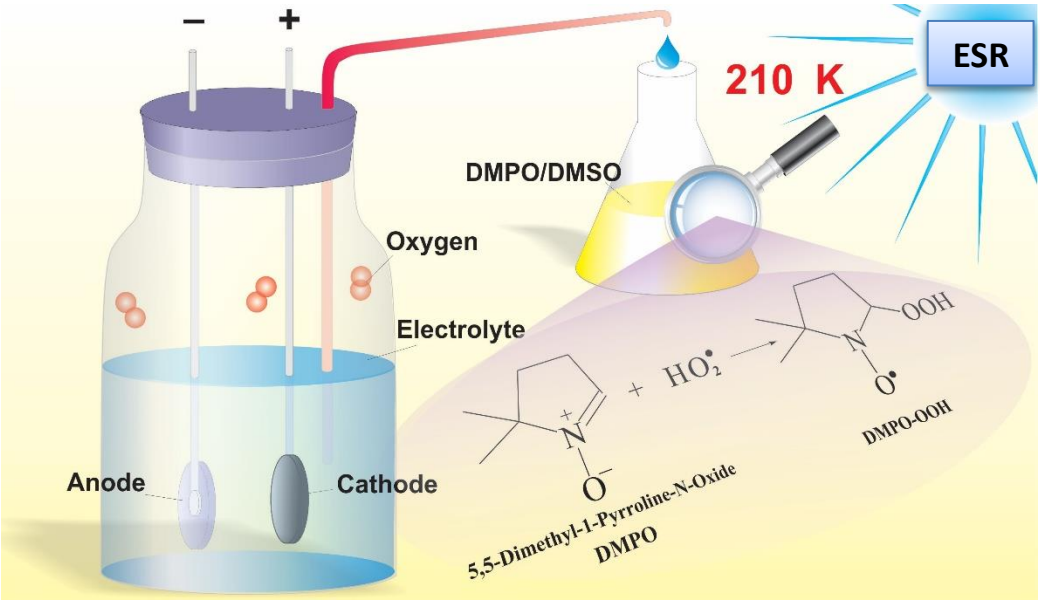

Figure 4.1 Schematic illustration of the Na-O_2 cell and *in-situ* electrolyte extraction of HO_2 radicals and/or carbon based radicals at 210 K. The low temperature stabilizes the radicals and allows their study by electron spin resonance spectroscopy.

ESR, a radical-sensitive technique, paired with 5,5-dimethyl-pyrroline N-oxide (DMPO) spin traps has been used to investigate short-lived superoxide radicals.[72] By forming relatively stable DMPO-OOH adducts (i.e., DMPO-HO_2), the solubilized superoxide species can be readily trapped by DMPO.[73] This allows for ESR investigations of the superoxide species in the electrolyte. Recently Cao *et al.* performed ESR studies on cathodic reactions in Li-O_2 cells by adding DMPO directly into the cell.[74] However, the ongoing degradation of DMPO-OOH adducts during discharge at room temperature complicates the resulting ESR spectra and obscures the underlying mechanisms.[75] In this study 100 µL of NaOTf salt electrolyte was extracted *in-situ* from an Na-O_2 glass cell operating during discharge or charge at various stages of electrochemical cycling and quickly cold-trapped at 210 K via reaction with 500 µL of 0.1 M

DMPO in dimethyl sulfoxide (DMSO), as illustrated in **Figure 4.1**. The ESR spectrum of the super-cooled solution was immediately measured by an X-band continuous-wave (CW) ESR spectrometer. The temperature of 210 K was chosen to suppress side reactions and facilitate tuning of the ESR cavity. The morphological changes of the products at the same points corresponding to the ESR spectral collection were investigated in parallel using a LEO 1530 field-emission SEM, by extraction of the carbon diffusion layer cathode from the glass cell.

4.3 Applicability of the ESR Spin-Trap Technique

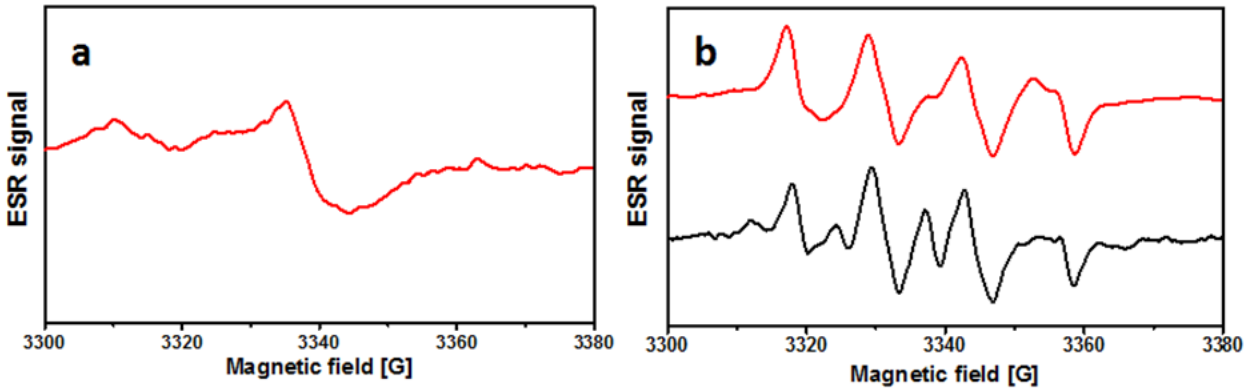

Figure 4.2 (**a**) ESR spectrum obtained after immersing a discharged cathode containing solid NaO_2 crystals in 0.1 M DMPO/DMSO for 10 s at 210 K. (**b**) ESR spectra of 3 mM KO_2/DMSO mixed with 0.1 M DMPO/DMSO for 10 s (red) and 12 h (black) at 210 K.

Figure 4.2a shows the ESR spectrum of a 0.1 M DMPO/DMSO solution after immersing a discharged cathode with solid NaO_2 products in it for 10 seconds. This spectrum is different from the four peak pattern of the DMPO-OOH adducts shown in **Figure 4.2b** (red spectrum) and literature. The observed signal in **Figure 4.2a** is likely due to the paramagnetic NaO_2 particles and carbon fibers that remained in the sample after the cathode was removed. This result is of

great importance as it indicates that solid NaO_2 products do not react with DMPO in DMSO to form DMPO-OOH adducts.

Potassium superoxide (3 mM KO_2) in DMSO solution was prepared by dissolving commercial KO_2 in distilled DMSO solvent under an argon atmosphere. The resulting solution was mixed with the DMPO/DMSO solution and immediately transferred for ESR measurement at 210 K. The mixture was measured again at 210 K after a rest period of 12 h at room temperature. As shown in **Figure 4.2b**, the red curve of the quickly mixed sample shows the typical four-peak pattern of the DMPO-OOH adducts. However, additional peaks appear when the mixture is measured again after sitting at room temperature for 12 h (black curve). As reported in the literature, the metastable DMPO-OOH adducts slowly decay to more stable DMPO-OH adducts and 5,5-Dimethyl-2-pyrrolidone-N-oxyl (DMPOX), which may be responsible for the additional peaks.[75] To avoid these undesired compounds, all electrolyte samples were mixed with DMPO/DMSO solution at room temperature for 10 s, and ESR measurements of these samples were then immediately carried out at 210 K.

The results from **Figure 4.2** clearly show that the ESR technique coupled with DMPO spin traps is applicable to investigate the paramagnetic superoxide radical.

4.4 Nucleation and Growth of NaO_2 from Electrolyte

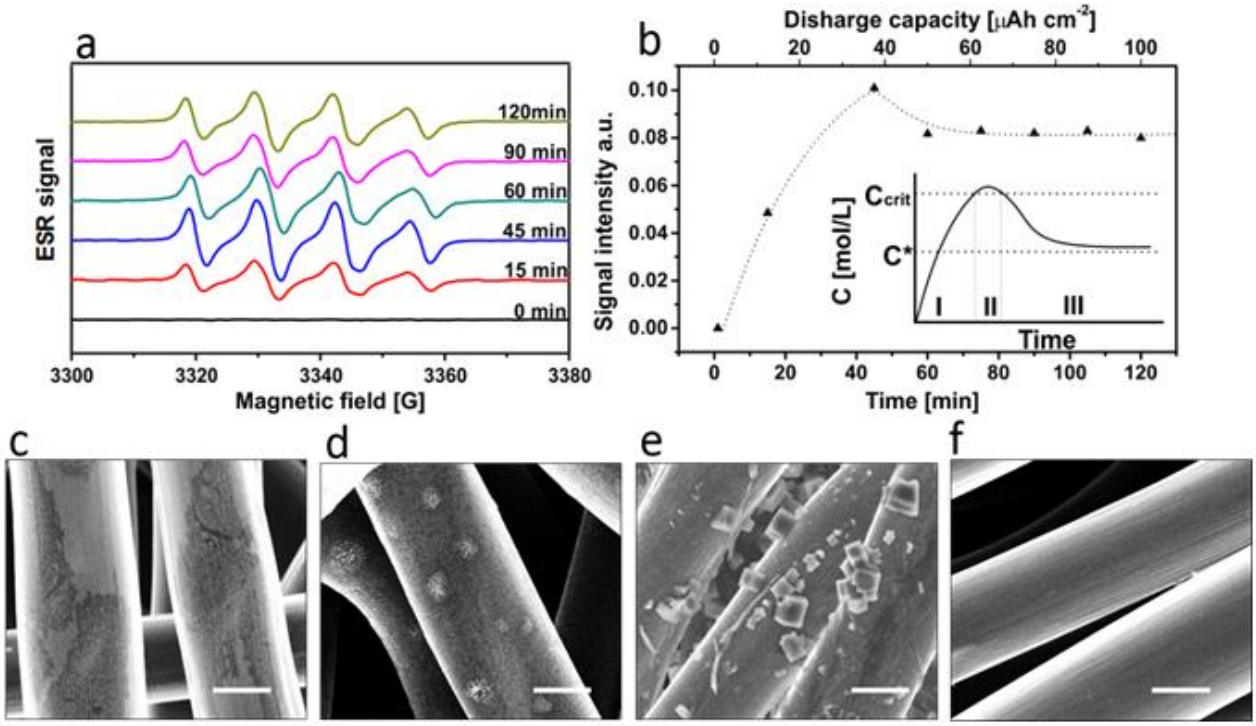

Figure 4.3 (**a**) ESR spectra of the NaOTf salt electrolyte at different discharge depths and (**b**) the corresponding intensity variation of the DMPO-OOH ESR signal. SEM images of the carbon-fiber cathode discharged for (**c**) 15 min, (**d**) 90 min, (**e**) 600 min, and (**f**) 15 min followed by immersing the cathode into NaOTf salt electrolyte for 1 h. The white bars indicate a length of 5 μm. The discharge current is 50 μA cm^{-2}.

Variations in the ESR spectra of the electrolyte and the morphological changes of the cathodic products upon discharge are shown in **Figure 4.3**. The electrolyte used contains 10 ppm of H_2O. Prior to discharge, the pristine electrolyte does not yield an ESR signal. Once ORR commences, a distinct ESR spectrum with four broad peaks appear as shown in **Figure 4.3a**. The observed ESR pattern and extracted hyperfine coupling constants (α_N=13.2 G, α_H^{β}=11.0 G, and α_H^{γ}=0.8 G) are the same as those of the reported DMPO-OOH.[76] This result proves the solubilization of superoxide as the hydroperoxyl (HO_2) species in the electrolyte. As discharge proceeds, the ESR pattern remains, while its intensity changes, indicating a variation of superoxide concentration.

Figure 4.3b shows that the intensity of the DMPO-OOH signal initially increases to a maximum value at a discharge time of 45 min. The signal is then followed by a short decrease that eventually reaches steady state. Such time-dependent changes have also been reported in the crystallization of other nanomaterials in solution, e.g., sulfur, silver halide, and magnetite. They are described by the classical LaMer mechanism.[77] Based on this mechanism, the curve representing the dissolved superoxide content can be divided into three regions as illustrated in the inset of **Figure 4.3b**.[78] (I) The solubilization of superoxide in the electrolyte leads to an initial increase of superoxide concentration. (II) Once a critical supersaturation, C_{crit}, is achieved, the superoxide, in the presence of sodium cations, undergoes "burst-nucleation," forming a large number of solid NaO_2 nanonuclei, which reduces the concentration of superoxide in solution. Subsequently, there is almost no nucleation occurring due to the low concentration of free superoxide in the electrolyte. (III) The newly formed superoxide moieties steadily diffuse to the nucleation sites of the NaO_2 nanoparticles. This leads to the epitaxial growth of NaO_2 crystals and stabilizes the concentration of superoxide at a low supersaturation, i.e., slightly higher than its solubility (C^*). The morphology changes of the cathodic products during discharge are shown in **Figure 4.3c-f**. At a short discharge time of 15 min (region I), film-like products are formed which partially cover the surface of the carbon fiber cathode (**Figure 4.3c**).

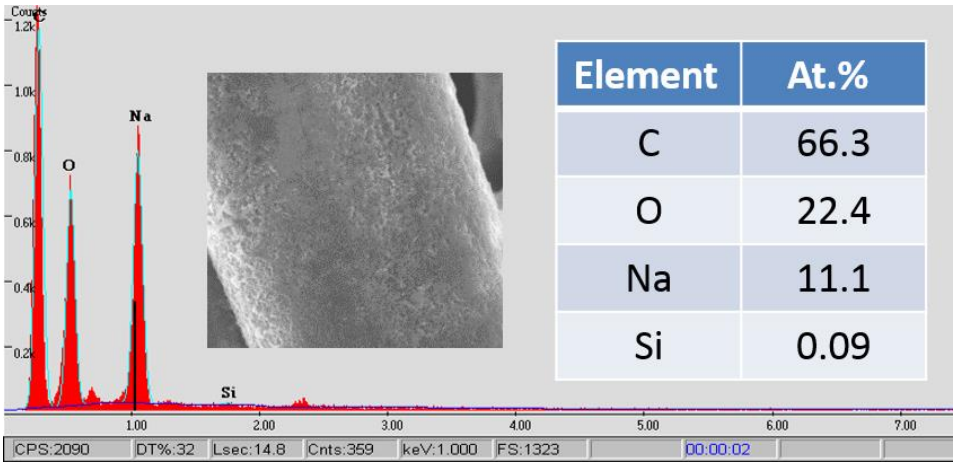

Element	At.%
C	66.3
O	22.4
Na	11.1
Si	0.09

Figure 4.4 Morphology and elemental composition of the discharged products formed at a discharge capacity of 2 mAh cm^{-2} analyzed by EDX.

The EDX result presented above (**Figure 4.4)** of the film-like discharge products formed at a discharge capacity of 2 mAh cm^{-2} clearly show a Na:O atomic ratio of 1:2 in the film products. This ratio indicates that the film products are composed of NaO_2. By association, the film products observed at a short discharge time of 15 min (**Figure 4.3c**) are also believed to be that of NaO_2. After immersing the cathode that was discharged for 15 min into pristine electrolyte for 1 h without polarization, the NaO_2 films dissolved, and the bare surface of the cathode was revealed (**Figure 4.3f**). This indicates slow dissolution of surface superoxide. Recently, such NaO_2 thin films have been proven to be highly insulating.[79] Thus, accelerating the dissolution of superoxide to eliminate the formation of NaO_2 films is critical to improve the discharge capacity and lower the charge overpotential. As the discharge proceeds to 90 min (region III), the entire cathode is covered by an NaO_2 film. More importantly, a number of spot-like particles are found deposited on the cathode (**Figure 4.3d**). These particles are likely the NaO_2 nuclei as predicted by the LaMer mechanism. After a discharge time of 600 min, these NaO_2 nuclei grow to micrometer-sized NaO_2 cubic crystals (**Figure 4.3e**),[15] kinetically driven by the proton phase

transfer catalytic process. This experimental observation conclusively shows that solution-mediated superoxide transport leads to the nucleation and growth of NaO_2 crystals upon discharge.

4.5 Water-Assisted Superoxide Transfer

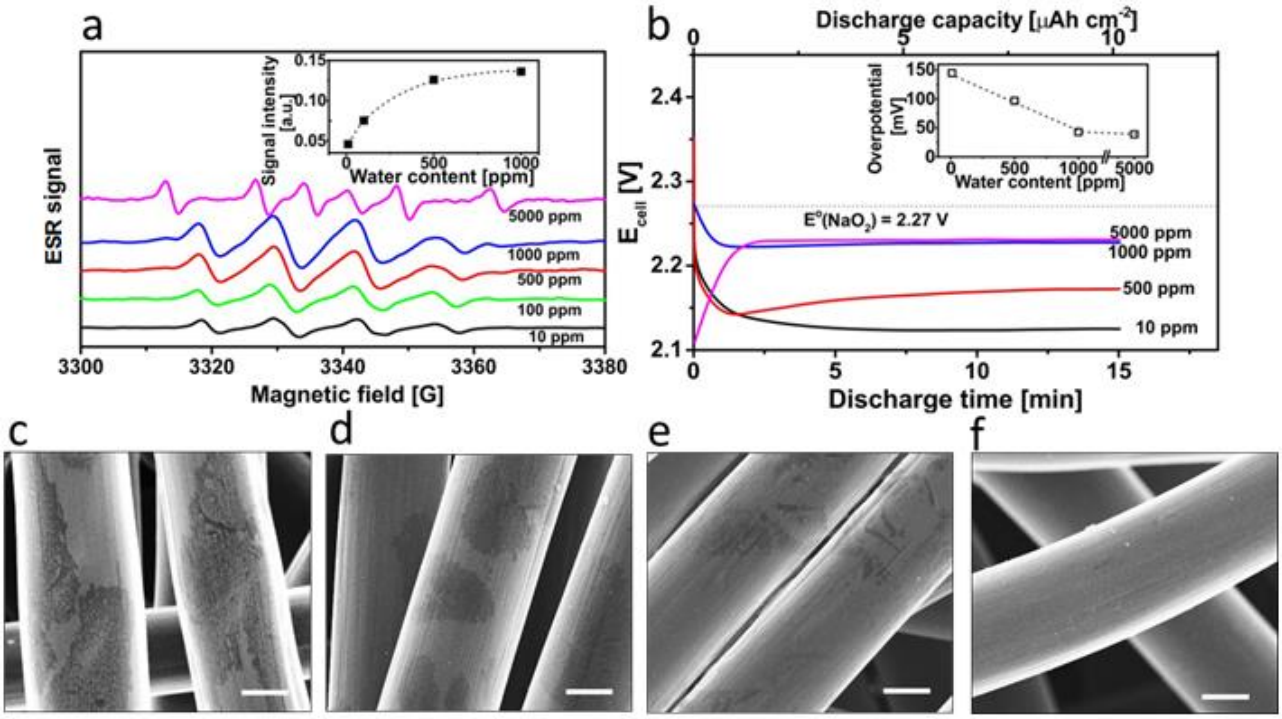

Figure 4.5 (**a**) Effects of H_2O content on the ESR spectra of discharged NaOTf salt electrolytes, and (**b**) the discharge curves of Na-O_2 cells at a constant discharge time of 15 min. Insets: the intensity changes of DMPO-OOH ESR signal and the discharge overpotential changes of cells as a function of H_2O concentration, respectively. SEM images of the discharged cathodes using NaOTf salt electrolytes with H_2O concentrations of (**c**) 10 ppm, (**d**) 100 ppm, (**e**) 500 ppm, and (**f**) 1000 ppm. The white bars indicate a length of 5 μm. A constant discharge current of 50 μA cm^{-2} was applied.

Figure 4.5 shows the effects of H_2O concentration on the solubilized superoxide species and the morphology of the cathode with a short discharge time of 15 min. With an increase of H_2O content, less NaO_2 film is found on the cathode (**Figure 4.5c-f**). Instead, more superoxide is detected in the electrolyte via the enhanced signal of the DMPO-OOH adduct (**Figure 4.5a**).

Based on the Noyes-Whitney equation, the poor solubility and low diffusion coefficient of NaO_2 in the electrolyte with 10 ppm of H_2O likely leads to the slow dissolution of NaO_2.[79] However, with the increase of H_2O content, the superoxide anion - being a strong Brønsted base - readily abstracts a proton from H_2O forming the soluble HO_2 intermediate, as suggested in the literature.[80]

4.6 ESR Evidence for Carbon-Centered Organic Radicals on Reduction

When an ultrahigh H_2O concentration of 5000 ppm is used for the electrolyte, the ESR spectrum of the discharged electrolyte changes to a six-peak pattern. This pattern has very different hyperfine values compared to that of the DMPO-OOH pattern, indicating the formation of other radicals (**Figure 4.5a**). The hyperfine splitting values of $\alpha_N = 14.1$ G and $\alpha_H = 21.3$ G indicate carbon-centered radicals, as shown below (**Figure 4.6**).[81]

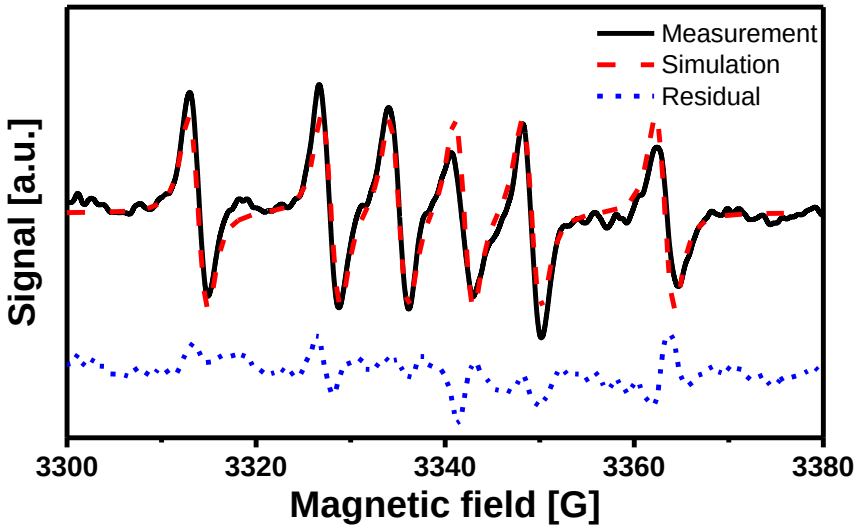

Figure 4.6 Measured and simulated ESR spectra of NaOTf salt electrolyte discharged for 15 min in the presence of 5000 ppm of H_2O. Black solid line indicates the measurement, red dotted line indicates the simulation, and blue dotted line indicates the residual pattern of the simulation.

Large amounts of HO_2, well known as a chemically reactive radical, will cause hydrogen abstraction from the glyme solvent, thus forming carbon-centered radicals as suggested in the literature.[36] The presence of these radicals indicates the decomposition of the electrolyte. Accordingly, only low quantities of H_2O (< 500 ppm) can be tolerated in Na-O_2 cells.

4.7 Solution-Mediated NaO_2 Oxidation

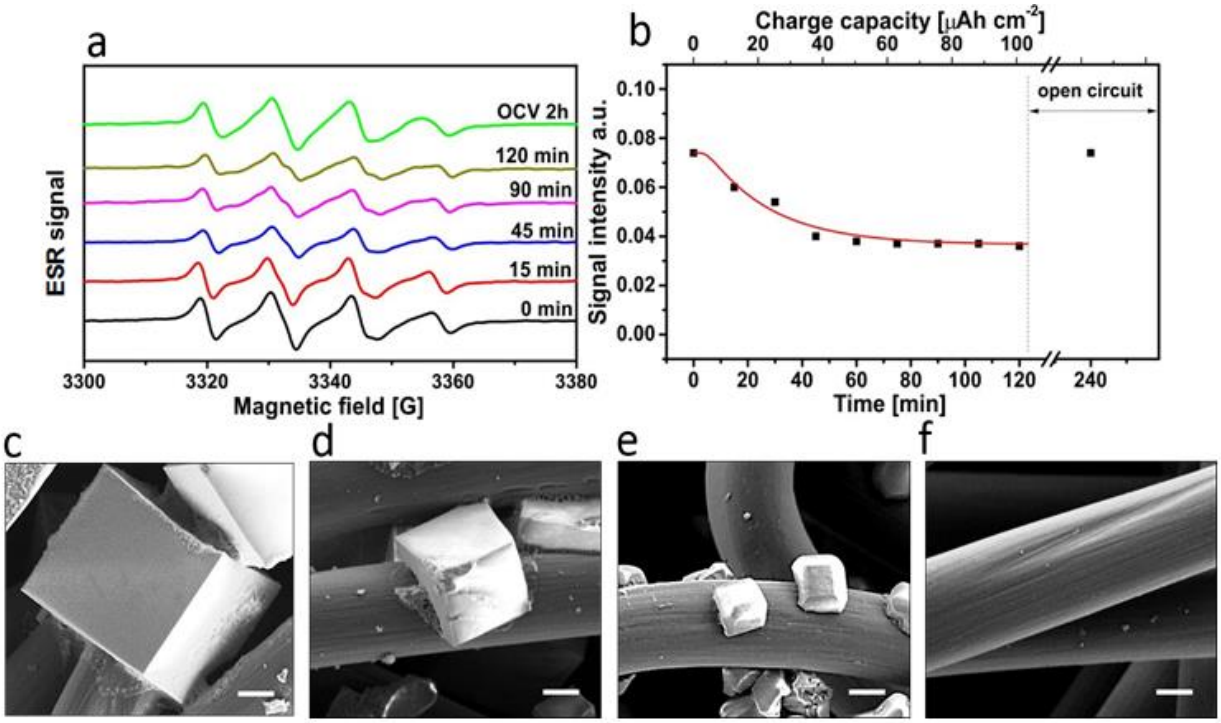

Figure 4.7 (**a**) ESR spectra of the NaOTf salt electrolyte at different charge depths and (**b**) the changes in intensity of DMPO-OOH signal upon charge. Morphology of cathodes charged for (**c**) 0 min, (**d**) 90 min, (**e**) 1200 min, and (**f**) 3.5 V (~2160 min). Note: the cathodes were pre-discharged to 2 mAh cm^{-2} and were then used for charge studies. The white bars indicate a length of 5 µm. The charge current is constant at 50 µA cm^{-2}.

For charging studies, carbon cathodes pre-discharged to 2 mAh cm^{-2} were used. Prior to charge, the electrolyte containing 10 ppm of H_2O shows the ESR spectrum of the DMPO-OOH adducts (**Figure 4.7a**). As expected, the HO_2 formed on discharge is not consumed (it is a catalyst). As presented in **Figure 4.7b**, on charge the intensity of the DMPO-OOH signal decreases and then reaches steady state after 45 min of charge. It indicates that the charge reaction consumes the superoxide in the electrolyte.

Upon the interruption of charge, NaO_2 crystals continuously dissolve in the electrolyte until an equilibrium state, i.e., its solubility, is achieved. The intensity of the DMPO-OOH adduct signal thus returns to its initial value after the cathode rests at open circuit conditions for 2 h (**Figure 4.7b**).

Figure 4.7c-f shows the morphology changes of the cathodic products upon charge. The dissolution of NaO_2 diminishes the size of the cubic crystals. At a charge time of 1200 min, the edges of NaO_2 particles are preferentially dissolved, likely due to their higher surface energy.[43] After charging the Na-O_2 cell up to 3.5 V, NaO_2 cubes are fully oxidized, revealing a bare cathode (**Figure 4.7f**). The Na-O_2 cell shows a typical coulombic efficiency of 90 % due to parasitic reactions and loss of superoxide within the cell.[16]

4.8 Effect of High Water Contents on Charge

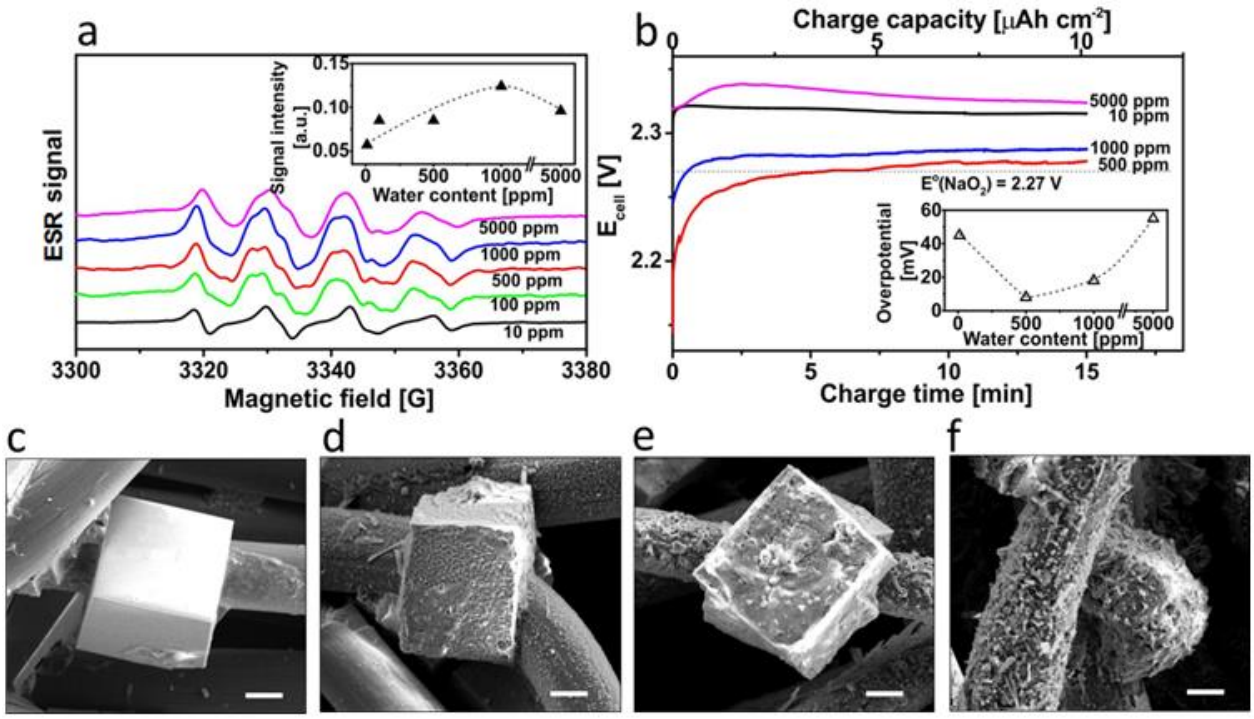

Figure 4.8 (**a**) Effects of H_2O concentrations on the ESR spectra of charged NaOTf salt electrolytes and (**b**) the charge curves of Na-O_2 cells at a constant charge time of 15 min. Insets show the intensity changes of DMPO-OOH ESR signal and the charge overpotential changes of cells as a function of H_2O content, respectively. Morphology of cathodes charged for 15 min using NaOTf salt electrolytes with H_2O concentrations of (**c**) 10 ppm, (**d**) 500 ppm, (**e**) 1000 ppm, and (**f**) 5000 ppm. The white bars indicate a length of 5 μm. A constant charge rate of 50 μA cm^{-2} was applied.

With increasing H_2O concentration (up to 1000 ppm), larger ESR signals of the DMPO-OOH adduct are observed. This indicates more superoxide is present in the electrolyte **(Figure 4.8a**). This result also suggests that H_2O improves the solubilization of superoxide during charge. Furthermore, the charge overpotential of the cell using an electrolyte with 500 ppm of H_2O is ~30 mV lower than that of the electrolyte with 10 ppm of H_2O (**Figure 4.8b**). However, the charge overpotential rises when the H_2O concentration is higher than 500 ppm. **Figure 4.8c-f** shows that the increase of H_2O content roughens the surface of NaO_2 cubic crystals. In addition,

the carbon fibers are fully covered with flake-like particles when the H_2O concentration is 5000 ppm. These particles were identified as sodium acetate and sodium peroxide dihydrate, as shown below (**Figure 4.9**). Thus, the enhanced solubilization of superoxide by H_2O triggers the decomposition of the electrolyte during charge.

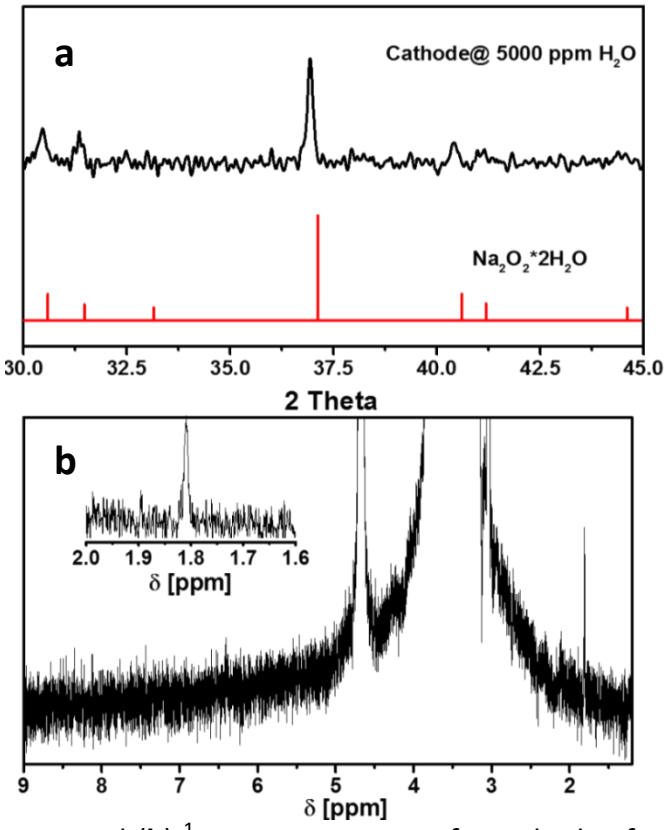

Figure 4.9 (**a**) XRD pattern, and (**b**) ^{1}H-NMR spectrum of a cathode after 15 min charge in the presence of 5000 ppm of H_2O.

4.9 ESR Evidence of Oxygen-Centered Organic Radicals on Oxidation

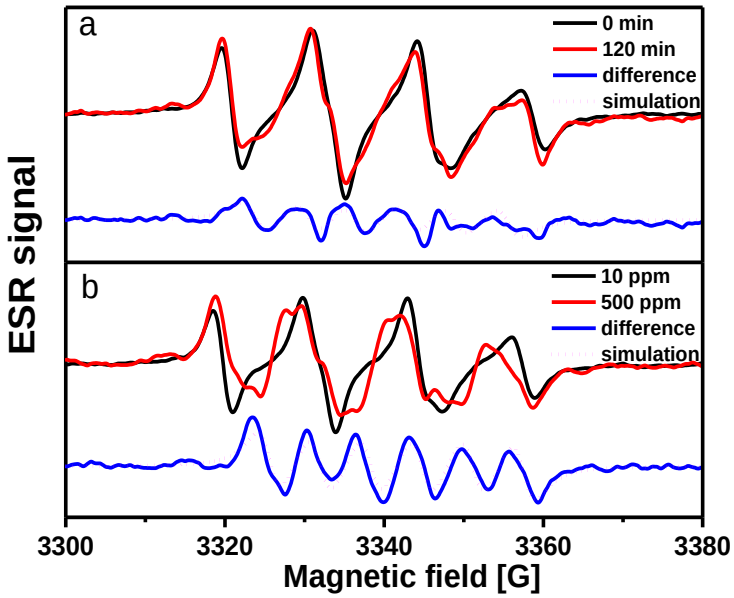

Figure 4.10 (**a**) Comparison of ESR spectra of NaOTf salt electrolyte samples with 10 ppm of H_2O charged for 0 min (black curve) and 120 min (red curve). The blue solid curve is the resulting spectrum obtained by subtracting the ESR signal of 120 min charged electrolyte from that of 0 min charged electrolyte. The dotted magenta curve is the simulation of the subtracted spectrum. (**b**) Comparison of ESR spectra of NaOTf salt electrolyte samples containing 10 and 500 ppm of H_2O charged for 15 min. Blue solid curve is the resulting spectrum obtained by subtracting the ESR signal of charged electrolyte with 500 ppm of H_2O from that of charged electrolyte containing 10 ppm of H_2O. The dotted magenta curve is the simulation of the subtracted spectrum.

Figure 4.10 compares the normalized ESR spectra of the electrolyte samples containing 10 ppm of H_2O charged for 0 min and 120 min as well as the electrolyte samples with 10 ppm and 500 ppm of H_2O charged for 15 min. The spectrum with either longer charge time or higher H_2O concentration in the electrolyte presents a distorted ESR pattern when compared to that of the DMPO-OOH adduct, which indicates another radical species is formed under these conditions. Subtraction of the sets of measured spectra shows identical ESR patterns (blue curves) with six equally distanced peaks. The simulated ESR spectra (dotted magenta curves) with simulation parameters of α_N = 12.8 G and α_H = 6.4 G show good agreement to the subtracted spectra. The

hyperfine coupling strengths obtained from the simulations suggest that the paramagnetic species responsible for the observed signals are likely alkyl oxygen-centered radicals (RO•).[73]

Consistent with these results, Adams *et al.* recently demonstrated that glyme-based solvents decompose and form alkyl oxygen-centered radicals.[82] The results in **Figure 4.10** indicate that the formation of RO• radicals requires either long charge times or high H_2O contents. Khetan *et al*. suggested, based on their simulations, that the rate of solvent degradation is determined by the acidity of the solvents (pK_a) and the concentration of superoxide in the electrolyte.[83] With the electrolyte containing 10 ppm of H_2O, a long time may be required to achieve a sufficiently high content of superoxide, due to its limited dissolution rate. However, such concentration of superoxide may easily be obtained in the presence of high H_2O contents. This result implies that solution processes greatly influence the reversibility of Na-O_2 cells. Clearly, more work is needed to prevent the decomposition of aprotic solvents by superoxide.

4.10 Conclusions

The observation of the ESR signal of DMPO-HO_2 in the NaOTf salt electrolyte with 10 ppm of H_2O conclusively shows the solubilization of superoxide *via* hydroperoxyl radicals. Increasing H_2O content leads to a greatly enhanced DMPO-HO_2 ESR signal, indicative of higher HO_2 concentration. Once a critical supersaturation is achieved, nucleation and growth of NaO_2 cubic crystals on the cathode, as observed by SEM, follows the classical LaMer mechanism. On charge the reverse occurs; accordingly, the NaO_2 crystals shrink in size, while the diminished intensity of the DMPO-HO_2 signal indicates consumption of superoxide in the electrolyte. These findings

show that the charge pathway involves the dissolution of NaO_2 through the soluble hydroperoxyl intermediate.

The results therefore provide direct evidence of soluble hydroperoxyl species in the Na-O_2 cell, and, furthermore, their reactions with glyme to form both carbon-centered and oxygen-centered organic radicals are revealed. These results enable insight into the decomposition of glyme-based electrolytes. A better understanding into the solution-mediated oxygen reaction mechanism is required. Future studies should be directed to explore other phase transfer catalysts with higher efficiency and to develop chemically stable electrolytes, both liquid and solid.

5 Limitations on the Rechargeability of Na-O_2 Batteries

5.1 Introduction

Although Na-O_2 cells present an improved chemical reversibility in comparison to their Li-O_2 cousins, the cycling stability of Na-O_2 cells is still far from the requirement for commercialization. Hartmann *et al.* reported that after 10 cycles the capacity of Na-O_2 cells dropped to less than 10 % of their initial capacity on the first cycle.[15] Clearly, more efforts are required to improve the cycling performance of Na-O_2 cells.

The primary causes for the poor cycling performance of Na-O_2 cells are still under debate. Research groups including Wu *et al.* report that the growth of sodium dendrites reach the cathode by penetrating through the separator and cause an internal short circuit, which terminates the cell.[45] In accordance, they propose that the growth of sodium dendrites is the main cause for Na-O_2 cell failure. In contrast, research groups including Janek *et al.* propose that carbon cathode corrosion and decomposition of aprotic electrolytes, which result in the surface passivation of the cathode, are the main causes for early termination of Na-O_2 cells.[19]

Research groups worldwide are interested in achieving outstanding cyclability in the Na-O_2 system; accordingly, it is critical to determine the primary causes for cell failure. In this study, the degradation factors of Na-O_2 cells were examined. The results demonstrate that sodium dendrite growth, carbon cathode corrosion, and decomposition of electrolyte all contribute to cell termination.

5.2 Growth of Sodium Dendrites

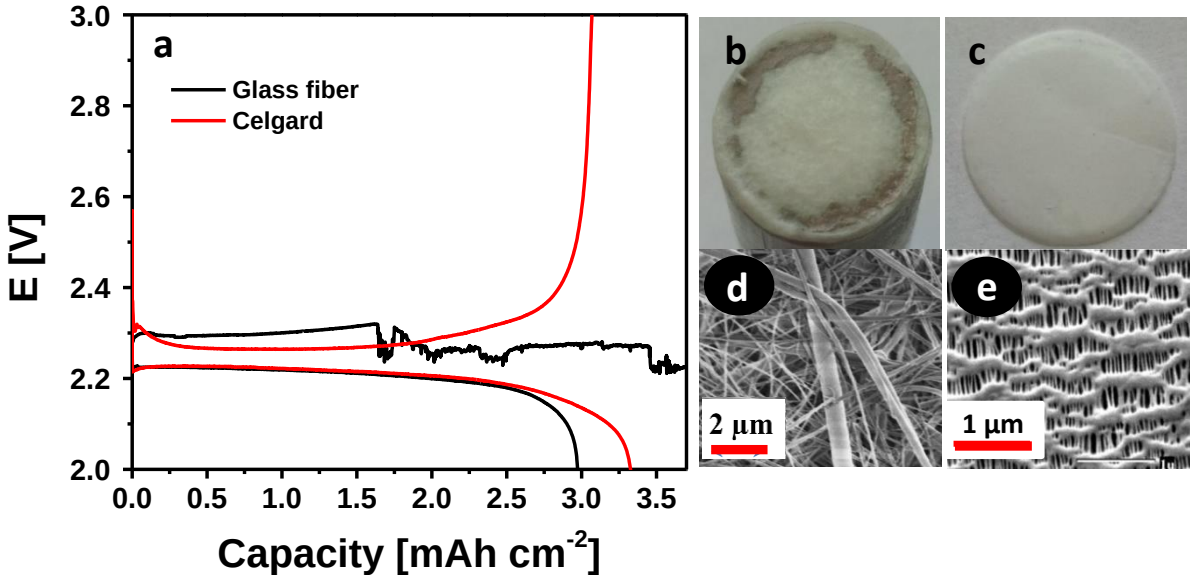

Figure 5.1 (**a**) First discharge-charge curves of Na-O_2 cells with glass fiber or Celgard separators using NaOTf salt electrolyte at 200 µA cm^{-2} with discharge and charge cut-off voltages of 2 V and 3 V, respectively. Pictures of (**b**) glass fiber and (**c**) Celgard separators after first charge. Morphology of (**d**) glass fiber and (**e**) Celgard separators prior to use.

Glass fiber separators composed of silicate have been widely used due to their good chemical stability, high porosity, and low cost. As shown in **Figure 5.1a** (black curve), the Na-O_2 cell using a glass fiber separator presents a unique charge profile, i.e., a stable charge plateau followed by a strong voltage fluctuation. Interestingly, the cell continues charging. After disassembling this cell, sodium dendrites are found on the cathode side of the separator (**Figure 5.1b**). The voltage fluctuation observed is identical to that reported by Wu.[45] They reveal that on charge the uneven deposition of sodium metal on the sodium electrode causes the formation of sodium dendrites, which grow through the glass fiber separator and ultimately contact the cathode. After the short circuit is established, large current flows through the dendrites. This current generates sufficient heat to then melt the sodium dendrites; accordingly, the dendrites' contact

with the cathode is cut off, and the cell is restored to its previous working charge potential. However, this sequence of events continues upon placing charge into the battery and, therefore, results in the observed voltage fluctuation.[84] As a result, cells using glass fiber separators could not be cycled.

Celgard® polypropylene film is another type of separator, which has been widely used in commercial batteries. Surprisingly, the cell using a Celgard separator allows for a more stable discharge and charge profile, as shown in **Figure 5.1a** (red curve). Furthermore, there are no visible sodium dendrites on the cathode side of the Celgard separator after a full charge to 3V (**Figure 5.1c**). Comparing **Figure 5.1d** and **e**, Celgard separators possess lower porosity, ~40 %, and smaller pore sizes, ~50 nm, than those of glass fiber separators (with porosity > 90 % and pore sizes > 1 μm). Therefore, the compact structure of the Celgard separator may mitigate sodium dendrite growth through the separator layer, thereby reducing the possibility of short circuits and voltage fluctuations. However, long term cycling would still result in dendrite formation through the separator.

5.3 Cathode Degradation

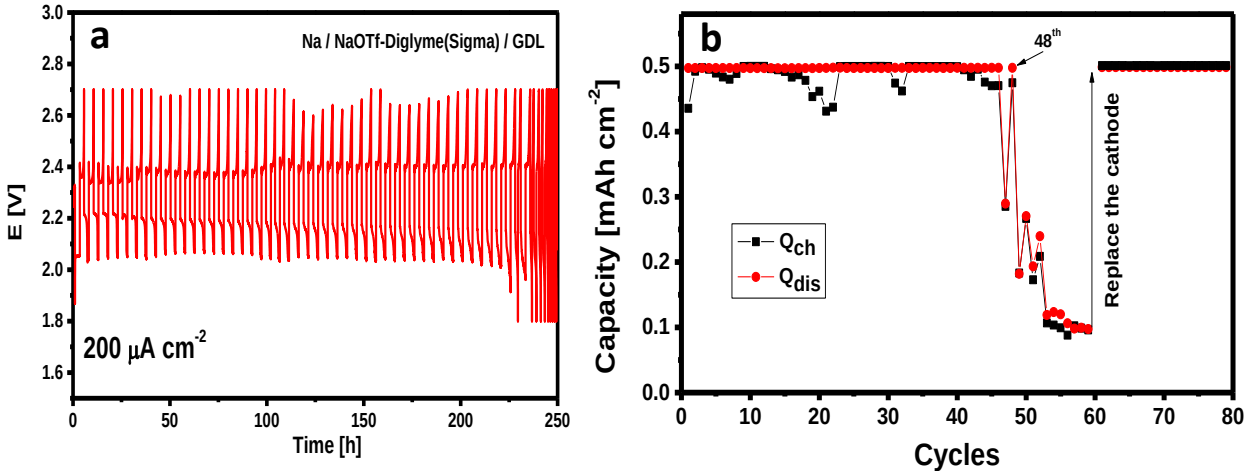

Figure 5.2 (**a**) Cycling performance of an Na-O_2 cell using two Celgard separators, GDL cathode, and NaOTf salt electrolyte at 200 μA cm^{-2} with a capacity limit of 0.5 mAh cm^{-2}. (**b**) Discharge (filled red circles) and charge (filled black circles) capacities, of the same Na-O_2 cell, as a function of the cycle. Note: The used GDL cathode is replaced with a new GDL cathode at the 60^{th} cycle.

Figure 5.2a shows the cycling performance of an Na-O_2 cell at a current density of 200 μA cm^{-2} with a capacity limit of 0.5 mAh cm^{-2}. The voltage of the charge plateau remains at approximately 2.4 V during cycling, whereas the voltage of the discharge plateau slowly decreases, indicating cell degradation. As presented in **Figure 5.2b**, the cell capacity starts to decrease at the 48^{th} cycle and drops to less than 0.1 mAh cm^{-2} after the 60^{th} cycle. By replacing the used cathode with a fresh GDL cathode, while keeping all other variables the same, the cell capacity resumes to its initial value, i.e., 0.5 mAh cm^{-2}. For comparison, two other Na-O_2 cells were equivalently cycled, and upon cell death the used Celgard separators from one cell were replaced with new separators, and the used anode from the other cell was replaced with a new anode. However, upon cycling, the capacity of these two cells remained low. This evidence suggests that the termination of the Na-O_2 cell using Celgard separators, in this study, is due to

cathode degradation, as opposed to dendrite formation. The following section characterizes the composition of the degraded cathode.

5.4 Evidence of Cathode Passivation

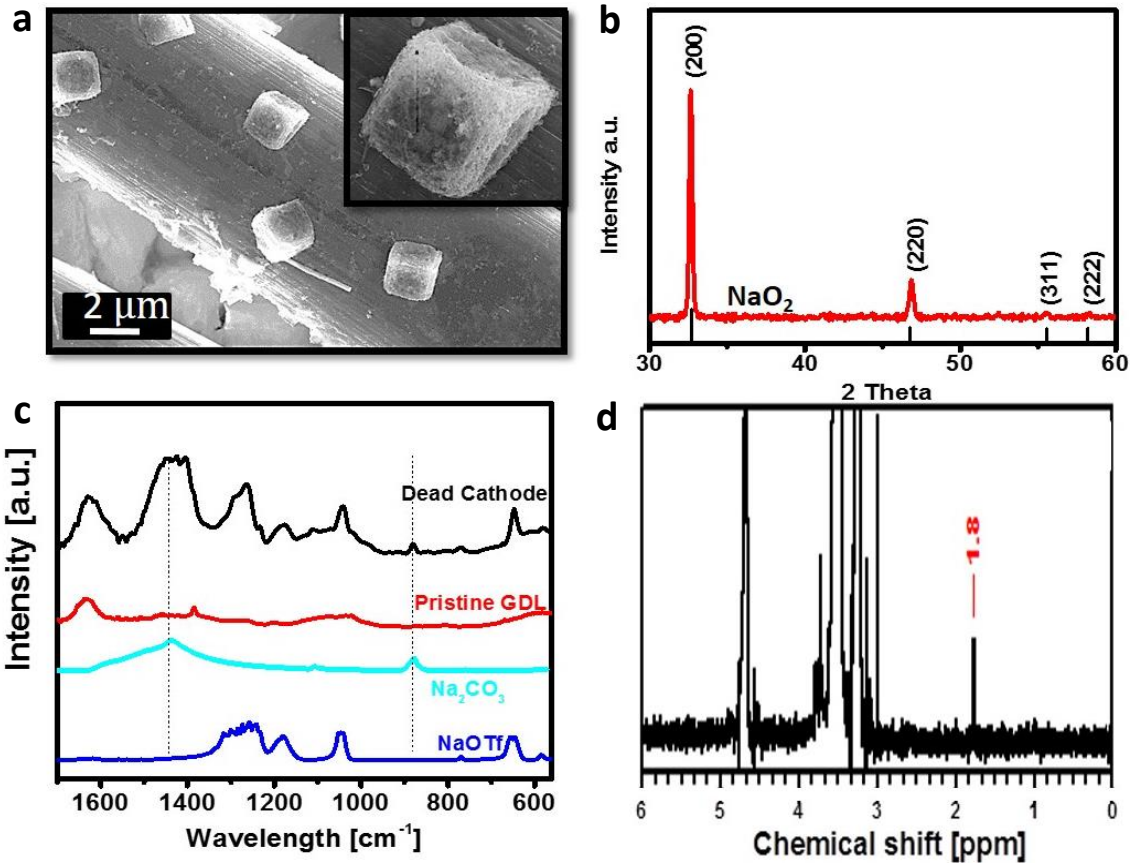

Figure 5.3 (**a**) SEM image and (**b**) X-ray diffraction pattern of the degraded GDL cathode from the Na-O_2 cell using two Celgard separators, GDL cathode, and NaOTf salt electrolyte, which was cycled for 60 cycles at 200 µA cm^{-2} with a capacity limit of 0.5 mAh cm^{-2}. (**c**) IR spectrum of the degraded cathode with NaOTf, Na_2CO_3, and pristine GDL references. (**d**) H^1-NMR spectrum of the degraded cathode.

Figure 5.3a shows the morphology of the GDL cathode after 60 cycles. Although the Na-O_2 cell has been charged to an oxidation potential of 3 V prior to cell disassembly, a number of cube-shaped NaO_2 crystals still remain on the surface of the carbon cathode, as proven by the XRD

result (**Figure 5.3b**). No other crystalline by-products are observed. It is important to note that both residual NaO_2 crystals and carbon fibers were covered with amorphous film-like products. As shown in **Figure 5.3c** and **d**, the thin film is determined to be a mixture of sodium carbonate and acetate species. As demonstrated in **Chapter 1**, the corrosion of the carbon cathode by superoxide forms the sodium carbonate species, while superoxide attack on an ether-based electrolyte forms the sodium acetate species.[38] During discharge, the deposition of these surface insulating by-products on the carbon cathode may increase the cell impedance and limit the oxygen reduction reaction, which would result in the observed rising discharge overpotential (**Figure 5.2a**). Upon charge, these insoluble by-products likely restrict the solution-mediated oxidation process, which would lead to the observed incomplete removal of NaO_2 crystals (**Figure 5.3a**).[85]

5.5 Conclusions

In this study, the failure mechanisms of Na-O_2 cells were investigated. The growth of sodium dendrites causes fatal short circuits and is even observed on the first cycle. However, through the substitution of glass fiber separator with Celgard polypropylene separator, the growth of sodium dendrites is somewhat impeded. As a result, the cycle life of Na-O_2 cells may be extended using Celgard polypropylene separators. Nonetheless, Na-O_2 cells using Celgard separators also fail. The termination of these cells likely resulted from superoxide-induced electrolyte decomposition and carbon corrosion as the resulting decomposition products were observed to passivate the cathodes. More efforts are needed to explore stable electrolytes and cathode materials.

6 Future Prospective

As highlighted in **Chapter 5**, the primary factors for Na-O_2 cell failure are due to decomposition of organic electrolytes and corrosion of carbon cathodes. Armed with the above knowledge, I highlight the need for both chemically stable electrolytes and cathodes.

6.1 Towards a Stable Electrolyte

As revealed in **Chapter 4**, superoxide initiates hydrogen-abstraction based radical decomposition from the backbone of glyme solvents. Therefore, eliminating the possibility of hydrogen abstraction is key to stabilize the electrolyte and further improve the cycling performance of Li-O_2 and Na-O_2 cells. Below, three research directions are proposed.

Protected Aprotic Electrolytes. Adams *et al.* found that by substituting the backbone protons on DME solvents with methyl (-CH_3) protecting groups, the possibility of hydrogen-abstraction on β-carbons of DME backbones is eliminated. This approach was effective in inhibiting formate, oxalate, and carbonate formation on the carbon cathode.[82] However, adding protecting groups (i.e. methyl moieties and trimethylsilyl groups) to solvents undoubtedly increase the solvents' steric hindrance. Accordingly, lower oxygen diffusivity and weakened interaction with sodium or lithium ions result for these solvents. Therefore, future work should be directed to synthesizing protected aprotic solvents with good stability and fast mass and charge transportation.

Ceramic Solid Electrolytes. Solid electrolytes (SEs), e.g., $Na_{1+x}Zr_2Si_xP_{3-x}O_{12}$(NASICON), are more resistant toward peroxide and superoxide attack.[86] Due to the lack of hydrogen in SEs, no hydrogen abstraction based radical decomposition can occur. In addition, SEs can also effectively restrict the growth of lithium and sodium dendrites.[87] Although SEs feature innate advantages over non-aqueous electrolytes, drawbacks such as low ionic conductivities, inability to invoke PPTCs, and high interfacial resistances restrict their use. Accordingly, more research is required to examine the applicability of SEs in Li-O_2 and Na-O_2 cells.

Inorganic Molten Salt Electrolytes. Different from organic molten salts, i.e., ionic liquids, inorganic molten salts that lack hydrogen and carbon elements are proposed to be stable against superoxide. Recently, Giordani *et al.* reported an Li-O_2 cell using molten nitrate as the electrolyte at 150 ^{o}C and demonstrated improved cell reversibility and cyclability.[88] Nevertheless, more research is needed to verify the stability of inorganic molten salts.

6.2 Towards a Stable Cathode

As mentioned in **Chapter 1**, the carbon cathode is prone to chemical corrosion by Li_2O_2 and NaO_2. Therefore, the substitution of carbon cathodes by non-carbonaceous materials shows great promise to improve the stability of alkali metal-oxygen cells. Below, two groups of carbon-free materials are proposed.

Chemically Stable Metal Materials. Bruce *et al.* used metallic gold as the cathode for non-aqueous Li-O_2 cells, and it accounted for a highly reversible Li-O_2 cell with 95% capacity retention for 100 cycles.[59] Other cost-effective metal materials, e.g., titanium and nickel, should be further examined as they may present more promising properties than those of carbon cathodes.

Conducting Metal Oxide Materials. Transparent conducting oxides (TCOs), due to their good electrical conductivity and chemical stability (resistant to oxidation), have recently been gaining momentum in battery research.[89] It has recently been reported that Li-O_2 cells using ruthenium/ indium tin oxide cathodes show good cyclability over 50 cycles without distinguishable decay.[90] Accordingly, other oxidation-resistant TCOs, e.g., fluorine doped tin oxide and fluorine doped zinc oxide, should be further examined as they also may be suitable substitutions for carbon cathodes.

7. Conclusions

Based on the results presented in this thesis, the four questions listed in **Chapter 1** will be answered.

7.1 Mechanism of NaO_2 Growth: PPTC-Induced Solution-Mediated Pathway

Through monitoring the superoxide concentration in the electrolyte during discharge, the growth of NaO_2 crystals was proven to proceed through a solution-mediated pathway, as opposed to a surface-conductive pathway. Key to the findings was coupling the technique of cold spin traps - to stabilize the dissolved superoxide species in the electrolyte for ESR analysis - with parallel SEM investigations. The results conclusively demonstrate that the transport of superoxide from the cathode to the electrolyte leads to the nucleation and growth of the NaO_2 discharge product. By tracking the variation of superoxide content in the electrolyte on discharge, the crystallization of cubic NaO_2 crystals was found in agreement with the classical LaMer mechanism of nucleation and growth (**Figure 4.3b**). In addition, the changes in superoxide content on charge (**Figure 4.7**) demonstrated that charge proceeds through the reverse solution processes. Foremost, the solution-mediated pathway is almost exclusively driven by the presence of proton phase transfer catalysts (PPTCs), e.g., H_2O, as they readily solubilize superoxide via HO_2 and accelerate solution-mediated superoxide transport (**Figure 4.5** and **Figure 4.8**). The growth and dissolution of cube-shaped NaO_2 crystals observed in Na-O_2 cells were therefore a result of these unique reversible solution-mediated processes.

7.2 Discharge Products of Na-O_2 Cells: Water Determined Discharge Products

The selectivity of discharge products in Na-O_2 cells was determined by the H_2O content in the electrolyte. Contents of H_2O less than 10 K ppm favoured the formation of NaO_2, whereas large contents of H_2O, greater than 10 K ppm, tune the discharge product to $Na_2O_2{\cdot}2H_2O$ (**Figure 3.9**). Mechanisms that may explain these results are proposed below:

$$H_2O + O_2^{\bullet -} \leftrightarrows HO_2^{\bullet} + OH^- \quad \text{R1}$$

$$HO_2^{\bullet} + Na^+ \leftrightarrows NaO_2^{\bullet} + H^+ \quad \text{R2}$$

At low contents of H_2O, the surface superoxide reversibly reacts with H_2O in solution and yields a small amount of HO_2 (R1). HO_2 converts to NaO_2 via metathesis on encounter with Na^+ ions (R2). The dynamic equilibrium of R1 and R2 may contribute to the better chemical reversibility observed for Na-O_2 cells, when NaO_2 is the discharge product.

$$H_2O + O_2^{\bullet -} \rightarrow HO_2^{\bullet} + OH^- \quad \text{R3}$$

$$HO_2^{\bullet} + HA \rightarrow H_2O_2 + A^{\bullet} \quad \text{R4}$$

$$H_2O_2 + 2OH^- + 2Na^+ \rightarrow Na_2O_2 \cdot 2H_2O \quad \text{R5}$$

In contrast, the presence of high contents of H_2O may shift the equilibrium (R3) in favour of the products, thereby forming a large amount of HO_2. As shown in R4, these HO_2 radicals (being chemically reactive) may abstract a hydrogen from the solvent (HA) and form H_2O_2 and carbon-centered radicals ($A^{\bullet}$) (**Figure 4.6**). Finally, H_2O_2 is converted to $Na_2O_2{\cdot}2H_2O$ via hydro-peroxylation, as shown in R5. Such an irreversible reaction pathway may result in the poor reversibility observed for Na-O_2 cells, when $Na_2O_2{\cdot}2H_2O$ is the discharge product.

7.3 Mechanism of Electrolyte Decomposition: Superoxide-Induced H-Abstraction

The decomposition of the electrolyte follows a radical decomposition mechanism. In this thesis a six-peak ESR spectrum was revealed and attributed to carbon-centered alkyl radicals, when high contents of H_2O (e.g., 5000 ppm) are present in the electrolyte during discharge (**Figure 4.6**). At high contents of H_2O, large amounts of hydroperoxyl species are present; accordingly, these species may readily abstract hydrogen from the solvent and initiate radical decomposition as previously speculated. To the best of my knowledge, this is the first experimental observation that conclusively shows that electrolyte decomposition occurs via radical reactions.

7.4 Primary Causes for the Failure of Na-O_2 Cells: Anodic Dendrite Growth and Cathodic Surface Passivation

The results suggest that both sodium dendrite growth and cathode passivation contribute to the Na-O_2 cell decay. However, the formation of sodium dendrites could be somewhat suppressed by using a Celgard separator with nano-sized pores (**Figure 5.1**). Nevertheless, Na-O_2 cells using Celgard separators also fail. The termination of these Na-O_2 cells likely resulted from carbon cathode surface passivation (**Figure 5.3**). Further studies into electrolyte and carbon cathode development are therefore required to truly attain a rechargeable Na-O_2 cell.

References

(1) Average Annual Emissions and Fuel Consumption for Gasoline-Fueled Passenger Cars and Light Trucks. https://www3.epa.gov/otaq/consumer (2008).

(2) Greenhouse Gas Emissions. https://www.ec.gc.ca/indicateurs-indicators (2016).

(3) Girishkumar, G.; McCloskey, B.; Luntz, A.; Swanson, S.; Wilcke, W. *J. Phys. Chem. Lett.* **2010,** *1*, 2193-2203.

(4) Electric Vehicles Market (on-road) (hybrid, plug-in, and battery) - Global Industry Analysis, Size, Share, Growth, Trends and Forecast, 2013 - 2019. http://www.transparencymarketresearch.com/electric-vehicles-market.html (2014).

(5) Yang, Z.; Zhang, J.; Kintner-Meyer, M.; Lu, X.; Choi, D.; Lemmon, J.; Liu, J. *Chem. Rev.* **2011,** *111*, 3577-3613.

(6) Nagaura, T.; Tozawa, K. *Prog. Batteries Solar Cells.* **1990,** *9*, 209.

(7) Nitta, N.; Wu, F.; Lee, J.; Yushin, G. *Mater. Today.* **2015,** *18*, 252-264.

(8) Goodenough, J.; Park, K. *J. Am. Chem. Soc.* **2013,** *135*, 1167-1176.

(9) Teki, R.; Datta, M.; Krishnan, R.; Parker, T.; Lu, T.; Kumta, P.; Koratkar, N. *Small.* **2009,** *5*, 2236-2242.

(10) Tarascon, J.; Armand, M. *Nature.* **2001,** *414*, 359-367.

(11) Tesla Reveals Model 3 Battery Pack Option, Battery Costs. http://www.valuewalk.com/2016/04/tesla-model-3-battery-pack-option (2016).

(12) Tesla Model S 90D. https://www.tesla.com/models/design (2016).

(13) Bruce, P. *Solid State Ion.* **2008,** *179*, 752-760.

(14) Lee, J.; Tai Kim, S.; Cao, R.; Choi, N.; Liu, M.; Lee, K.; Cho, J. *Adv. Energy Mater.* **2011,** *1*, 34-50.

(15) Hartmann, P.; Bender, C.; Vračar, M.; Dürr, A.; Garsuch, A.; Janek, J.; Adelhelm, P. *Nat. Mater.* **2013,** *12*, 228-232.

(16) McCloskey, B.; Garcia, J.; Luntz, A. *J. Phys. Chem. Lett.* **2014,** *5*, 1230-1235.

(17) Kraytsberg, A.; Ein-Eli, Y. *J. Power Sources.* **2011,** *196*, 886-893.

(18) Black, R.; Adams, B.; Nazar, L. *Adv. Energy Mater.* **2012,** *2*, 801-815.

(19) Hartmann, P.; Bender, C.; Sann, J.; Dürr, A.; Jansen, M.; Janek, J.; Adelhelm, P. *Phys. Chem. Chem. Phys.* **2013,** *15*, 11661-11672.

(20) Peng, Z.; Freunberger, S.; Hardwick, L.; Chen, Y.; Giordani, V.; Bardé, F.; Novák, P.; Graham, D.; Tarascon, J.; Bruce, P. *Angew. Chem.* **2011,** *123*, 6475-6479.

(21) Yang, J.; Zhai, D.; Wang, H.; Lau, K.; Schlueter, J.; Du, P.; Myers, D.; Sun, Y.; Curtiss, L.; Amine, K. *Phys. Chem. Chem. Phys.* **2013,** *15*, 3764-3771.

(22) Xia, C.; Waletzko, M.; Chen, L.; Peppler, K.; Klar, P.; Janek, J. *ACS Appl. Mater. Interfaces.* **2014,** *6*, 12083-12092.

(23) Laoire, C.; Mukerjee, S.; Abraham, K.; Plichta, E.; Hendrickson, M. *J. Phys. Chem. C.* **2010,** *114*, 9178-9186.

(24) Laoire, C.; Mukerjee, S.; Abraham, K.; Plichta, E.; Hendrickson, M. *J. Phys. Chem. C.* **2009,** *113*, 20127-20134.

(25) McCloskey, B.; Scheffler, R.; Speidel, A.; Girishkumar, G.; Luntz, A. *J. Phys. Chem. C.* **2012,** *116*, 23897-23905.

(26) Hummelshøj, J.; Blomqvist, J.; Datta, S.; Vegge, T.; Rossmeisl, J.; Thygesen, K.; Luntz, A.; Jacobsen, K.; Nørskov, J. *J. Chem. Phys.* **2010,** *132*, 071101.

(27) Ganapathy, S.; Adams, B.; Stenou, G.; Anastasaki, M.; Goubitz, K.; Miao, X.; Nazar, L.; Wagemaker, M. *J. Am. Chem. Soc.* **2014,** *136*, 16335-16344.

(28) Li, Y.; Yadegari, H.; Li, X.; Banis, M.; Li, R.; Sun, X. *Chem. Commun.* **2013,** *49*, 11731-11733.
(29) Kim, J.; Lim, H.; Gwon, H.; Kang, K. *Phys. Chem. Chem. Phys.* **2013,** *15*, 3623-3629.
(30) Jian, Z.; Chen, Y.; Li, F.; Zhang, T.; Liu, C.; Zhou, H. *J. Power Sources.* **2014,** *251*, 466-469.
(31) Liu, W.; Sun, Q.; Yang, Y.; Xie, J.; Fu, Z. *Chem. Commun.* **2013,** *49*, 1951-1953.
(32) Black, R.; Oh, S.; Lee, J.; Yim, T.; Adams, B.; Nazar, L. *J. Am. Chem. Soc.* **2012,** *134*, 2902-2905.
(33) Lu, Y.; Gallant, B.; Kwabi, D.; Harding, J.; Mitchell, R.; Whittingham, M.; Shao-Horn, Y. *Energy Environ. Sci.* **2013,** *6*, 750-768.
(34) Mizuno, F.; Nakanishi, S.; Shirasawa, A.; Takechi, K.; Shiga, T.; Nishikoori, H.; Iba, H. *Electrochem.* **2011,** *79*, 876-881.
(35) McCloskey, B.; Valery, A.; Luntz, A.; Gowda, S.; Wallraff, G.; Garcia, J.; Mori, T.; Krupp, L. *J. Phys. Chem. Lett.* **2013,** *4*, 2989-2993.
(36) Freunberger, S.; Chen, Y.; Drewett, N.; Hardwick, L.; Bardé, F.; Bruce, P. *Angew. Chem. Int. Ed.* **2011,** *50*, 8609-8613.
(37) McCloskey, B.; Speidel, A.; Scheffler, R.; Miller, D.; Viswanathan, V.; Hummelshøj, J.; Nørskov, J.; Luntz, A. *J. Phys. Chem. Lett.* **2012,** *3*, 997-1001.
(38) Black, R.; Shyamsunder, A.; Adeli, P.; Kundu, D.; Murphy, G.; Nazar, L. *ChemSusChem.* **2016**. DOI: 10.1002/cssc.201600034.
(39) Lee, B.; Kim, J.; Yoon, G.; Lim, H.; Choi, I.; Kang, K. *Chem. Mater.* **2015,** *27*, 8406-8413.
(40) Ortiz-Vitoriano, N.; Batcho, T.; Kwabi, D.; Han, B.; Pour, N.; Yao, K.; Thompson, C.; Shao-Horn, Y. *J. Phys. Chem. Lett.* **2015,** *6*, 2636-2643.
(41) Sun, Q.; Yang, Y.; Fu, Z. *Electrochem. Commun.* **2012,** *16*, 22-25.
(42) Kang, S.; Mo, Y.; Ong, S.; Ceder, G. *Nano Lett.* **2014,** *14*, 1016-1020.
(43) Lee, B.; Seo, D.; Lim, H.; Park, I.; Park, K.; Kim, J.; Kang, K. *Chem. Mater.* **2014,** *26*, 1048-1055.
(44) Sharon, D.; Afri, M.; Noked, M.; Garsuch, A.; Frimer, A.; Aurbach, D. *J. Phys. Chem. Lett.* **2013,** *4*, 3115-3119.
(45) Bi, X.; Ren, X.; Huang, Z.; Yu, M.; Kreidler, E.; Wu, Y. *Chem. Commun.* **2015,** *51*, 7665-7668.
(46) Bender, C.; Jache, B.; Adelhelm, P.; Janek, J. *J. Mater. Chem. A.* **2015,** *3*, 20633-20641.
(47) Brett, C. *Electrochemistry: Principles, Methods, and Applications*. Oxford University Press Inc.: New York, 1994.
(48) G. Goldstein, D. Echlin, D. Joy, C. Fiori, E. Lifshin, *Scanning Electron Microscopy and X-ray Microanalysis*. Plenum Press: New York, 1981.
(49) Y. Waseda, E. Shinoda, *X-Ray Diffraction Crystallography*. Springer Science & Business Media: Berlin, 2011.
(50) J. W. Akitt. *NMR and Chemistry*. CRC Press: Boca Raton, 2000.
(51) Bielski, B.; Cabelli, D.; Arudi, R.; Ross, A. *J. Phys. Chem. Ref. Data.* **1985,** *14*, 1041-1100.
(52) Maiti, G.; Baerns, M. *Appl. Catal. A. Gen.* **1995,** *127*, 219-232.
(53) Howells, R.; Mc Cown, J. *Chem. Rev.* **1977,** *77*, 69-92.
(54) Williams, D.; Grand, J.; Miller, R. *J. Am. Chem. Soc.* **1956,** *78*, 5150-5155.
(55) Cheary, R.; Coelho, A. *J. Appl. Crystallogr.* **1992,** *25*, 109-121.
(56) Sofina, N.; Peters, E.; Jansen, M. *Z. Anorg. Allg. Chem.* **2003,** *629*, 1431-1436.
(57) Aetukuri, N.; McCloskey, B.; García, J.; Krupp, L.; Viswanathan, V.; Luntz, A. *Nat. Chem.* **2015,** *7*, 50-56.
(58) McCloskey, B.; Scheffler, R.; Speidel, A.; Bethune, D.; Shelby, R.; Luntz, A. *J. Am. Chem. Soc.* **2011,** *133*, 18038-18041.

(59) Thotiyl, M.; Freunberger, S.; Peng, Z.; Bruce, P. *J. Am. Chem. Soc.* **2012,** *135*, 494-500.
(60) Sawyer, D.; Valentine, J. *Acc. Chem. Res.* **1981,** *14*, 393-400.
(61) Chin, D.; Chiericato Jr, G.; Nanni Jr, E.; Sawyer, D. *J. Am. Chem. Soc.* **1982,** *104*, 1296-1299.
(62) Foote, C.; Valentine, J.; Greemberg, A.; Liebman, J. *Active Oxygen in Chemistry. Structure Energetics and Reactivity in Chemistry.* Chapman & Hall, New York: 1995.
(63) Bender, C.; Hartmann, P.; Vračar, M.; Adelhelm, P.; Janek, J. *Adv. Energy Mater.* **2014,** *4*.
(64) J Johnson, L.; Li, C.; Liu, Z.; Chen, Y.; Freunberger, S.; Ashok, P.; Praveen, B.; Dholakia, K.; Tarascon, J.; Bruce, P. *Nat. Chem.* **2014,** *6*, 1091-1099.
(65) Meini, S.; Solchenbach, S.; Piana, M.; Gasteiger, H. *J. Electrochem. Soc.* **2014,** *161*, A1306-A1314.
(66) Das, S.; Lau, S.; Archer, L. *J. Mater. Chem. A.* **2014,** *2*, 12623-12629.
(67) Schwenke, K.; Metzger, M.; Restle, T.; Piana, M.; Gasteiger, H. *J. Electrochem. Soc.* **2015,** *162*, A573-A584.
(68) Wandt, J.; Jakes, P.; Granwehr, J.; Gasteiger, H.; Eichel, R. *Angew. Chem.* **2016,** *128*, 7006-7009.
(69) Gowda, S.; Brunet, A.; Wallraff, G.; McCloskey, B. *J. Phys. Chem. Lett.* **2012,** *4*, 276-279.
(70) Mo, Y.; Ong, S.; Ceder, G. *Phys. Rev. B.* **2011,** *84*, 205446.
(71) Yadegari, H.; Li, Y.; Banis, M.; Li, X.; Wang, B.; Sun, Q.; Li, R.; Sham, T.; Cui, X.; Sun, X. *Energy Environ. Sci.* **2014,** *7*, 3747-3757.
(72) Villamena, F.; Merle, J.; Hadad, C.; Zweier, J. *J. Phys. Chem. A.* **2005,** *109*, 6089-6098.
(73) Pieta, P.; Petr, A.; Kutner, W.; Dunsch, L. *Electrochim. Acta.* **2008,** *53*, 3412-3415.
(74) Cao, R.; Walter, E.; Xu, W.; Nasybulin, E.; Bhattacharya, P.; Bowden, M.; Engelhard, M.; Zhang, J. *ChemSusChem.* **2014,** *7*, 2436-2440.
(75) Rosen, G.; Rauckman, E. *J. Mol. Pharmacol.* **1980,** *17*, 233-238.
(76) Harbour, J.; Hair, M. *J. Phys. Chem.* **1978,** *82*, 1397-1399.
(77) LaMer, V.; Dinegar, R. *J. Am. Chem. Soc.* **1950,** *72*, 4847-4854.
(78) Thanh, N.; Maclean, N.; Mahiddine, S. *Chem. Rev.* **2014,** *114*, 7610-7630.
(79) Hartmann, P.; Heinemann, M.; Bender, C.; Graf, K.; Baumann, R.; Adelhelm, P.; Heiliger, C.; Janek, J. *J. Phys. Chem. C.* **2015,** *119*, 22778-22786.
(80) Roberts, J.; Sawyer, D. *Isr. J. Chem.* **1983,** *23*, 430-438.
(81) Buettner, G. *Free Radic. Biol. Med.* **1987,** *3*, 259-303.
(82) Adams, B.; Black, R.; Williams, Z.; Fernandes, R.; Cuisinier, M.; Berg, E.; Novak, P.; Murphy, G.; Nazar, L. *Adv. Energy Mater.* **2015,** *5*, 1400867.
(83) Khetan, A.; Luntz, A.; Viswanathan, V. *J. Phys. Chem. Lett.* **2015,** *6*, 1254-1259.
(84) Aurbach, D.; Zinigrad, E.; Cohen, Y.; Teller, H. *Solid State Ion.* **2002,** *148*, 405-416.
(85) Landa-Medrano, I.; Pinedo, R.; Bi, X.; Ruiz de Larramendi, I.; Lezama, L.; Janek, J.; Amine, K.; Lu, J.; Rojo, T. *ACS Appl. Mater. Interfaces.* **2016**, DOI: 10.1021/acsami.6b06577.
(86) Li, F.; Kitaura, H.; Zhou, H. *Energy Environ. Sci.* **2013,** *6*, 2302-2311.
(87) Cao, C.; Li, Z.; Wang, X.; Zhao, X.; Han, W. *Front. Energy Res.* **2014,** *2*, 25.
(88) Giordani, V.; Tozier, D.; Tan, H.; Burke, C.; Gallant, B.; Uddin, J.; Greer, J.; McCloskey, B.; Chase, G.; Addison, D. *J. Am. Chem. Soc.* **2016,** *138*, 2656-2663.
(89) Kim, D.; Hwang, I.; Kwon, S.; Kang, H.; Park, K.; Choi, Y.; Choi, K.; Park, J. *Nano Lett.* **2007,** *7*, 3041-3045.
(90) Li, F.; Tang, D.; Chen, Y.; Golberg, D.; Kitaura, H.; Zhang, T.; Yamada, A.; Zhou, H. *Nano Lett.* **2013,** *13*, 4702-4707.